University of Glasgow

Pitman, Alex (2024) *A comparative study of proton exchange membranes: performance, stability and hydrogen crossover.* MRes thesis.

https://theses.gla.ac.uk/84729/

Copyright and moral rights for this work are retained by the author

A copy can be downloaded for personal non-commercial research or study, without prior permission or charge

This work cannot be reproduced or quoted extensively from without first obtaining permission from the author

The content must not be changed in any way or sold commercially in any format or medium without the formal permission of the author

When referring to this work, full bibliographic details including the author, title, awarding institution and date of the thesis must be given

Enlighten: Theses
https://theses.gla.ac.uk/
research-enlighten@glasgow.ac.uk


# A Comparative Study of Proton Exchange Membranes: Performance, Stability and Hydrogen Crossover

**2023 – 2024**

**Alex Pitman**

**Prof Mark D. Symes and Abdulhai Faqeeh**

# Declaration of Academic Integrity

University of Glasgow | School of Chemistry

## Declaration of Originality Form

This form **must** be completed and signed and submitted with all assignments.

Please complete the information below (using BLOCK CAPITALS).

Name ..... ALEX PITMAN

Student Number .....

Course Name ..... MRES CHEMISTRY

Assignment Number/Name ..... MRES CHEMISTRY RESEARCH PROJECT

**An extract from the University's Statement on Plagiarism is provided overleaf. Please read carefully THEN read and sign the declaration below.**

**I confirm that this assignment is my own work and that I have:**

- Read and understood the guidance on plagiarism in the Undergraduate Handbook, including the University of Glasgow Statement on Plagiarism ☑
- Clearly referenced, in both the text and the bibliography or references, **all sources** used in the work ☑
- Fully referenced (including page numbers) and used inverted commas for **all text quoted** from books, journals, web etc. (Please check with the Department which referencing style is to be used) ☑
- Provided the sources for all tables, figures, data etc. that are not my own work ☑
- Not made use of the work of any other student(s) past or present without acknowledgement. This includes any of my own work, that has been previously, or concurrently, submitted for assessment, either at this or any other educational institution, including school (see overleaf at 32.2) ☑
- Not sought or used the services of any professional agencies to produce this work ☑
- In addition, I understand that any false claim in respect of this work will result in disciplinary action in accordance with University regulations ☑

**DECLARATION:**

I am aware of and understand the University's policy on plagiarism and I certify that this assignment is my own work**,** except where indicated by referencing, and that I have followed the good academic practices noted above

Signed.....

# Abstract

Proton exchange membrane water electrolysis (PEMWE) presents itself as an attractive tool to support the renewable energy transition. By coupling these technologies together, a clean and environmentally friendly route to hydrogen production is created. Hydrogen can then act as an energy vector, delivering power areas where it is needed most. At the heart of the technology lies the proton exchange membrane (PEM) – a polymer that acts as a solid electrolyte, thus allowing protons to permeate through the device. The benchmark membrane is the Nafion™ brand, which has backbone similar to polytetrafluoroethylene (PTFE) and a long fluorinated carbon side chain capped with sulfonic groups. Aquivion® is another brand of membrane – similar to Nafion™, only that the side chain is shorter in length. Despite these membranes competing in identical markets, there are few existing comparative studies regarding their use in water electrolysis. The data that is available suggests the short side chain of Aquivion® yields optimal properties. Unfortunately, in recent months both of these membranes have been discontinued by many leading retailers, leaving researchers with no tried and tested membrane available for use.

This project investigated both of these issues. Aquivion® and Nafion™ were evaluated across three key parameters – performance, degradation rate and hydrogen crossover - and compared against an unbranded commercially available membrane. The results showed that the use of a short side chain membrane did not significantly vary device operation across the three key parameters, and also showed the unbranded membrane to perform at levels similar to the branded membranes. Ex-situ characterisation revealed the presence of membrane degradation after device operation. Future experiments could see the unbranded membrane being tested at timescales required in an industrial electrolyser.

# Table of Contents

# List of Abbreviations

| | |
|---|---|
| AEMWE | Anion Exchange Membrane Water Electrolysis |
| AWE | Alkaline Water Electrolysis |
| CCM | Catalyst Coated Membrane |
| CCS | Catalyst Coated Substrate |
| CL | Catalyst Layer |
| EIS | Electrical Impedance Spectroscopy |
| GDL | Gas Diffusion Layer |
| HER | Hydrogen Evolution Reaction |
| ICP-OES | Inductively Coupled Plasma – Optical Emission Spectroscopy |
| LSV | Linear Sweep Voltammetry |
| MEA | Membrane Electrode Assembly |
| MPL | Microporous Layer |
| OER | Oxygen Evolution Reaction |
| PEM | Proton Exchange Membrane |
| PEMWE | Proton Exchange Membrane Water Electrolysis |
| PFSA | Perfluorosulfonic Acid |
| PTFE | Poly Tetrafluoroethylene |
| SD | Standard Deviation |
| SEM | Scanning Electron Microscope |
| sPPS | Sulfonated Poly Phenylene Sulfone |

# 1. Introduction

On the 12th of December 2015, 195 countries met in Paris, France, and signed the first unified global agreement to tackle climate change. The treaty was the culmination of over 20 years of work by the United Nations Framework Convention on Climate Change, whose primary objective is to 'prevent dangerous anthropogenic interference with the climate system'[1]. It has been established that the best way to do this is to curb global mean temperature rise to well below 2 °C with respect to pre-industrial levels, by the turn of the new century[2]. The primary contributor to global warming is the emission of greenhouse gases, so by cutting these emissions to zero by 2060-75, it is proposed the warming of the planet can be sufficiently slowed[3]. Globally in 2022 49.7 Gt of carbon dioxide were released into the atmosphere, highlighting the extensive worldwide reform needed to reach zero emissions by 2060[4].

The biggest contributor to greenhouse gas emissions is the energy sector, which accounts for over 75 % of global emissions[5]. The current energy sector relies primarily on fossil fuels, which upon combustion release greenhouse gases into the atmosphere and contribute heavily to global warming. Due to rising human population and global economies, energy demand is at an all-time high - reaching 178,000 TWh for the first time in 2022[6]. The market shows no signs of slowing down and global energy consumption is predicted to double by 2050. Unless alternative energy resources are identified and harnessed sufficiently, the burning of fossil fuels is going to lead to a global climate disaster. Fossil fuels are a finite resource and although precise estimates cannot be calculated (due to the regular discovery of new reserves), it is expected that oil and gas supplies will run out within this lifetime. Unfortunately, coal reserves are still plentiful across the planet, meaning they will be a possible source of energy for many years to come. It is evident that a replacement energy source is urgently required to prevent a climate and economic disaster[7].

Renewable energy is an attractive solution to the aforementioned problems. It is classed as an infinite resource because it is harnessed from elements of the natural world like the sun, wind, and tide. By using technology to convert this energy into electricity, the world can be powered with a significant reduction in greenhouse gas emissions. Unfortunately, fossil fuels still dominate the global energy market at present as shown by Figure 1[6].

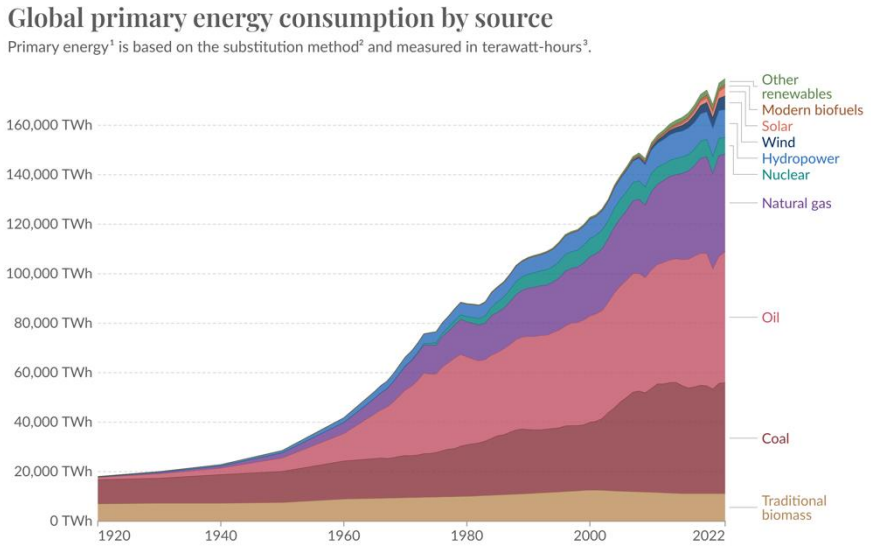


**Figure 1** – *Stacked line chart showing the breakdown of global energy consumption by energy source in Terawatt hours compared yearly. Sources include traditional biomass, coal, oil, natural gas, nuclear, hydropower, wind, solar, modern biofuels and other renewables*[6].

The figure shows that in 2022, only 13.3 % of global energy consumption was met by renewables – with hydropower contributing the greatest, followed by wind and then solar[6]. In coming years, wind and solar are expected to make notable market gains as device performance increases rapidly. Through investment in the research and development of renewable energy technology, many countries are taking significant strides towards meeting their end of the Paris Agreement. For example, Norway has spent decades investing in an extensive hydropower network, which harnesses the energy from rivers and fjords to meet 92% of the country's electivity demand[8].

Renewable energy depends on the natural world which is something that cannot be predicted or controlled. Windspeed, rainfall and sunlight are all intermittent resources and so if a country was solely reliant on renewable energy, there would undoubtedly be times where production falls short of demand and vice versa. Additionally, the areas rich in natural resource are often far from human population, which poses challenges in delivering energy to the areas it is needed most. It appears that renewable energy alone is not enough to replace fossil fuels – a carrier is required to store and transport the energy produced. Many believe batteries can help with this; however as they require large quantities of finite earth metals such as nickel, cobalt

and lithium, their uptake would lead to an future resource bottleneck. This has caused attention to turn to the most abundant resource on earth – water.

## 1.1. Hydrogen

The complete combustion of hydrogen yields two molecules of water and is presented below.

$$H_2 + \frac{1}{2} O_2 \rightarrow H_2O$$

With an energy density nearly triple that of petrol (120 MJ/kg vs 44 MJ/kg, respectively), it is clear why hydrogen is believed to be the solution to the global energy crisis. By releasing hydrogen from water through electrolysis powered by renewable energy, a fuel is harnessed from the most abundant resource on earth.

At present, hydrogen is not commonly used as a fuel - 51 % of global hydrogen is currently used in ammonia synthesis, 31 % is used in oil refining, 10 % in methanol production and 8 % in other applications[9]. Although hydrogen has a high energy density, its volumetric density is relatively low and due to the small particle size, it easily leaks out of containment vessels, presenting challenges with storage and transport. Additionally, hydrogen is currently produced primarily from fossil fuels, and so despite the fuel itself releasing no greenhouse gases, it's synthesis leads to the production of vast quantities. The primary means of hydrogen production are explored in Figure 2.

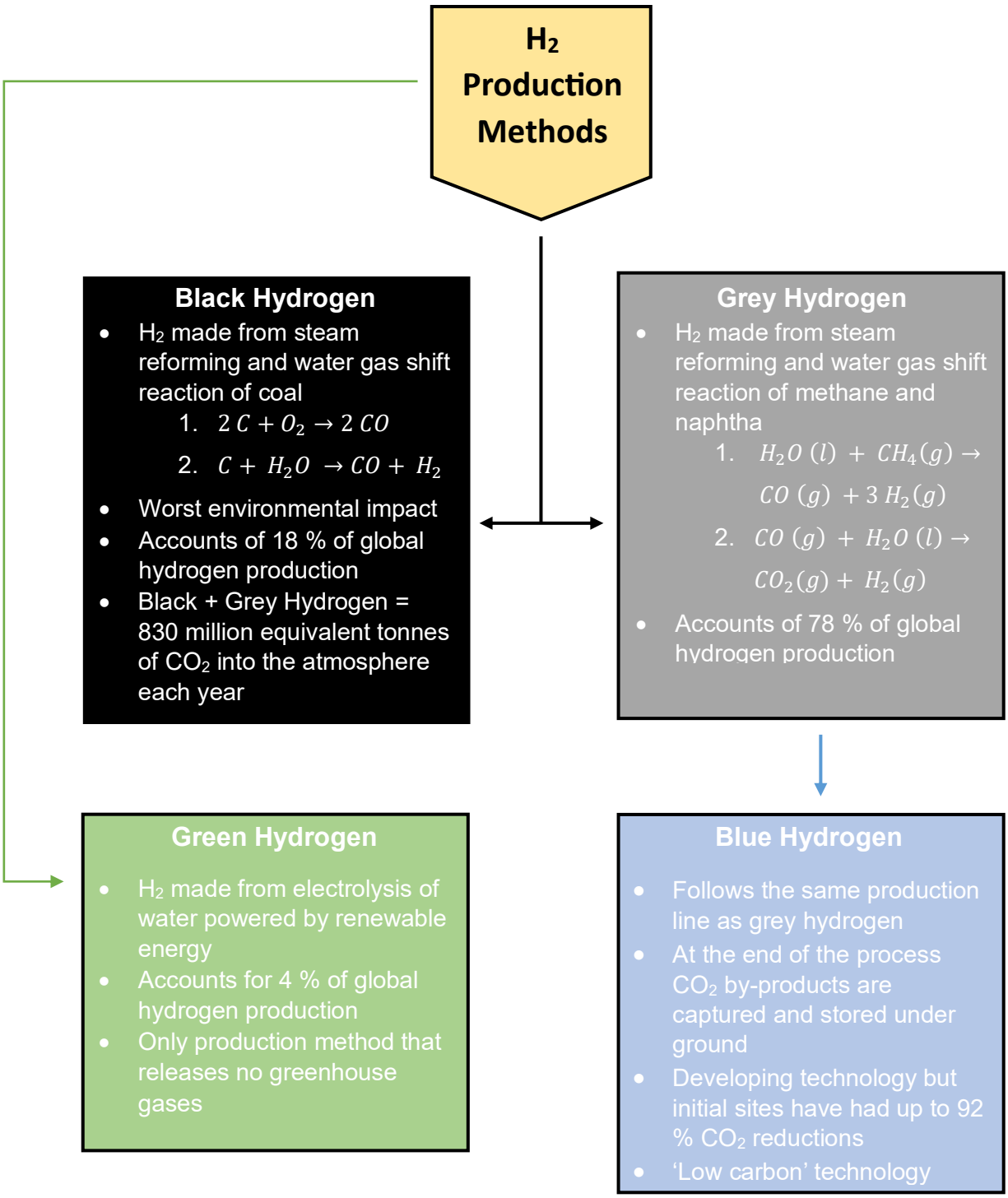


**Figure 2** – *Figure comparing common methods of hydrogen production globally*[9,10,11].

From Figure 2, it is shown that the only common means of hydrogen production that does not involve fossil fuels is green hydrogen. There are three main technologies which produce green hydrogen at low temperatures - alkaline water electrolysis (AWE), proton exchange membrane water electrolysis (PEMWE), and anion exchange membrane water electrolysis (AEMWE)[12].

Of these methods, AWE is the most mature and dominates the green hydrogen market. This is predicted to soon change as PEMWE technology reaches commercial application and AEMWE is a developing technology aiming to combine the advantages of both AWE and PEMWE. In order for the potential of hydrogen based fuels to be fully realised, further development of water electrolysis technology is required.

## 1.2. Fundamentals of Water Electrolysis

Water electrolysis can be used to produce hydrogen and oxygen gas in an electrochemical flow cell. A direct current is applied to a system, and at the anode oxygen gas is produced in a reaction known as the oxygen evolution reaction (OER). At the cathode hydrogen gas is produced via the hydrogen evolution reaction (HER). The combined electrochemical equation for these reactions is shown below.

$$H_2O\ (l) \rightarrow \frac{1}{2}O_2(g) + H_2(g)$$

The above shows that the reaction is entropically favourable as 1.5 moles of gaseous products are formed from 1 mole of liquid reactant. It is known that under standard conditions the enthalpy change ($\Delta H_{H2O}$) and entropy change ($\Delta S_{H2O}$) of this reaction is 285.84 kJ mol$^{-1}$ and 0.163 kJ mol$^{-1}$, respectively[13]. Given the high enthalpic requirement, at room temperature the reaction is thermodynamically unfavourable and also highly endothermic. Equation 1 can be used to calculate the Gibbs free energy ($\Delta G_{H2O}$) under standard conditions for the electrolysis of water.

(1) $$\Delta G = \Delta H - T\Delta S$$

This yields a value of $\Delta G_{H2O}$ = 237.35 kJ mol$^{-1}$. The positive Gibbs free energy shows that the reaction is non-spontaneous under standard conditions and is a highly energy intensive process. Given that $T\Delta S$ represents the thermal requirement of the reaction and $\Delta H$ remains near constant across all temperatures, it can be said that the Gibbs free energy represents the electrical energy required to complete the reaction[14]. This is highlighted in Figure 3[13].

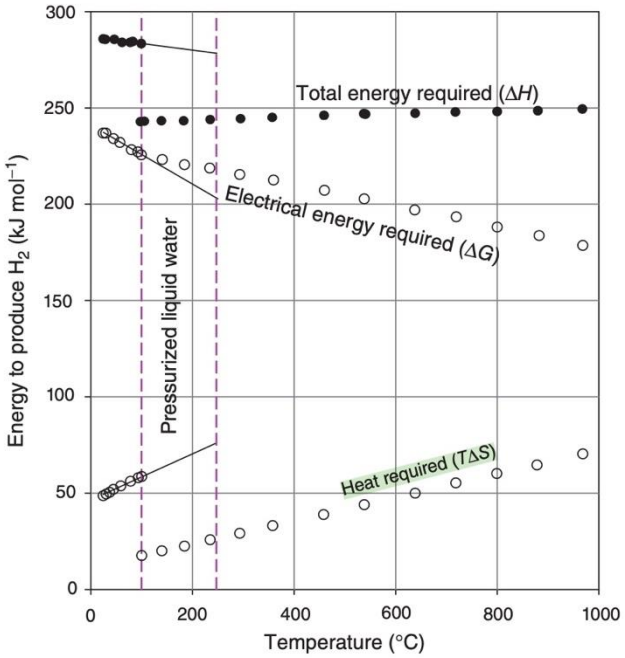


**Figure 3** – *Graph showing the effect of temperature (℃) on the different energy contributions required to produce $H_2$ from water electrolysis (kJ mol$^{-1}$). The total energy required (enthalpy) is represented by black dots, the upper white circles represent the electrical energy requirement (Gibbs free energy) and the lower white circles represent the thermal requirement of the reaction (entropy)*[13]*The enthalpy and entropy both decrease at 100 ℃ due to the change in state of water (from liquid to vapour)*[13].

Equation 1 and Figure 3 demonstrate that at 80 °C, the electrical energy required to complete the reaction is reduced to around 228 kJ mol$^{-1}$, demonstrating a reduction in the electrical energy required compared to operation at room temperature[13]. When the high cost of electricity is compared to thermal energy, it is clear why water electrolysis at elevated temperatures is desirable. Although some types of water electrolysis are performed at extremely high temperatures (*ca* 600 °C), the excessively high temperatures make the technology unfeasible in most applications.

Equation 2 can be used to determine the theoretical cell potential, which tells us the minimum required potential to complete a reaction.

(2) $$\Delta_r G = nFE_{cell}$$

Where $\Delta_r G$ is the Gibbs free energy of the reaction, n is the number of electrons transferred, F is Faraday's constant (96485 C mol$^{-1}$) and $E_{cell}$ is the theoretical cell potential. For the

electrolysis of water, this gives a value of $E_{cell}$ = 1.23 V under standard conditions. Within the cell, when electrons are flowing from the anode to the cathode they are met with internal resistance which causes the potential to drop. To combat this energy penalty, a larger operating potential is used. Additionally, overpotential is present in all electrochemical reactions due to the presence of a non-ideal system. It is described as the extra potential above the thermodynamically derived value needed to complete a reaction and reach a specific current density[15]. Both internal resistance and overpotential mean that the required voltage for a reaction to occur is often notably higher than $E_{cell}$. By providing an electrocatalyst, an alternative pathway with a reduced overpotential is made available, meaning lower potentials can be used to reach desired current density.

### 1.2.1. Alkaline Water Electrolysis

The first reports of alkaline water electrolysis were by Troostwijk and Deiman in 1789, and by 1900 it is estimated that there were over 400 industrial AWE plants worldwide[16]. However, the development of fossil fuels and cheap steam-reforming quickly replaced the technology as the leading method of hydrogen production, and its use was only continued in niche applications. AWE boasts very simple design principles, meaning since the birth of the technology minimal modifications have been required making it the most popular type of water electrolysis industrially.

The process works by electrolysing a concentrated (pH 14) alkaline solution - typically potassium hydroxide or sodium hydroxide. At the cathode, water is split by electrons to produce hydrogen gas and hydroxide ions. These anions pass through a diaphragm to reach the anode where they form oxygen gas. The HER and OER reactions are shown below.

$$\text{HER: } 2\,H_2O\,(l) + 2\,e^- \rightarrow H_2(g) + 2\,OH^-(aq)$$

$$\text{OER: } 2\,OH^-(aq) \rightarrow \frac{1}{2}O_2(g) + H_2O + 2\,e^-$$

Stainless steel electrodes containing nickel and nickel oxide electrocatalysts are found at the cathode and anode, respectively, due to low cost, high activity, and corrosion resistance in alkaline media[17]. Other non-noble metals such as cobalt and iron have been explored, however nickel delivers superior performance[18]. AWE devices tend to operate in the finite-gap

configuration, meaning the electrode and diaphragm are not in direct contact with each other. Figure 4 shows a simplified version of a working AWE device.

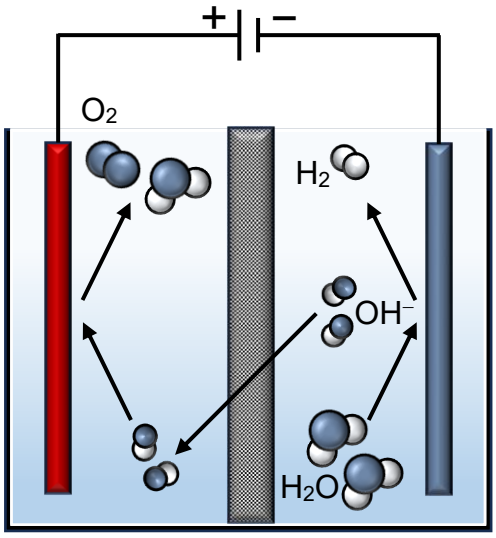


**Figure 4** – *A diagram of a conventional AWE device. At the cathode (blue) water is split into hydroxide ions and hydrogen gas. The hydroxide ions then permeate through the diaphragm to reach the anode (red) where they are converted to oxygen gas and water. Electrons flow through the external circuit to complete the process.*

Modern AWEs reap the benefits of a well-established industrial process and are capable of performing in the mega-watt output range. They are particularly useful for large scale hydrogen production – given lifetimes of over 120,000 hours are reported[19,20]. The devices also have relatively low operational costs as they run at temperatures between 70 – 90 °C and ambient pressure, while also being inexpensive to purchase due to the use of transition metal catalysts.

However, several factors currently inhibit the technology from reaching the 'gold-standard' of hydrogen production. The diaphragms used – traditionally asbestos, but now ceramic or microporous based – allow for hydrogen crossover at the anode[21]. This is caused by the pressure gradient within the system, where two moles of hydrogen gas are produced for each mole of oxygen gas, thus creating a potentially explosive atmosphere and also impure hydrogen (*ca* 99.9%). This process act to decrease device efficiency through the promotion of the reformation of water at both sides[19,22]. The devices also operate at low current densities between 0.2-0.4 A $cm^{-2}$ due to high internal resistance, meaning that plants must be large to produce a significant volume of product[23]. Additionally, the devices do not cope well with

fluctuating operating conditions - as would be expected when powered by a renewable resource[24].

These challenges manifest as bulky devices that are not compatible with the needs of a future hydrogen based economy, and so alternative routes to green hydrogen production must be explored.

### 1.2.2. Proton Exchange Membrane Water Electrolysis

PEMWE was first developed by General Electric in the 60's to address the shortcomings of AWE[16]. Water is fed into the anode where an electrical current oxidises water to form diatomic oxygen, releasing protons and electrons. The protons then then permeate through a membrane to the cathode where they meet with electrons to form diatomic hydrogen[25]. This process is summarised in the equation below.

$$\text{OER: } H_2O\ (l) \rightarrow 2\ H^+(aq) + \frac{1}{2} O_2(g) + 2\ e^-$$

$$\text{HER: } 2\ H^+(aq) + 2\ e^- \rightarrow H_2(g)$$

The media used is ultra-pure water between 70 – 90 °C[26]. The membrane is typically a polymer with a PTFE backbone and perfluorovinyl ether side chains capped by bulky sulfonate groups. This is known as a perfluorosulfonic acid (PFSA) membrane. When fully hydrated, the sulfonate groups become charged thus allowing for the selective permeation of protons. The cathode reaction has been fully optimised and is catalysed by platinum on carbon. At the anode, noble metals are used due to their superior properties under the high potential and oxidative conditions present. Iridium dioxide is favoured for its stability and ruthenium dioxide for its activity[27]. Figure 5 shows a schematic of a PEMWE device.

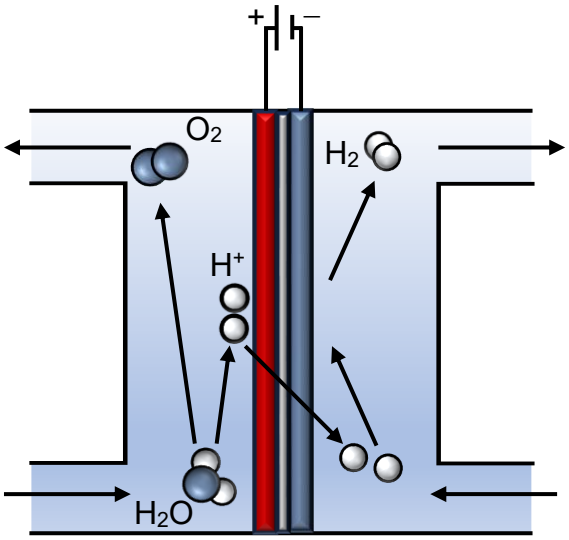


**Figure 5** – *A diagram of a working PEMWE device. At the anode (red) water is split to form protons and oxygen gas. The protons then permeate through the membrane to reach the cathode (blue) where they are combined to form hydrogen gas. Electrons flow through the external circuit to complete the process.*

PEMWE is favoured for providing solutions to the problems of AWE. Where alkaline water electrolysers report low current densities, these devices boast values of over 2 A $cm^{-2}$ – allowing for a significantly reduced size[28]. This is partially attributed to the zero-gap operating configuration – meaning that the membrane and electrodes are in direct contact which reduces the internal resistance. The product hydrogen is ultra-pure (*ca* 99.999%) thus eliminating safety concerns and costly product purification[25]. However, the driving force positioning PEMWE as a frontrunner over AWE is the rapid dynamic response time. The small electrolysers take seconds to adapt to operating load changes, whereas AWE devices take around 10 minutes. This highlights the suitability of PEMWE powered by renewable energy[28].

When the goal of storing renewable energy as fuel is considered, PEMWE poses many advantages over conventional AWE. Despite this, there are still many challenges which must be addressed before the technology is ready to fully compete with AWE.

Supply chain issues with the proton exchange membranes (PEMs) mean they are often unavailable or extremely costly. The use of iridium dioxide also poses a significant obstacle, as a recent study has shown present production would be unable to meet the demand of a large-scale PEMWE industry at current loading masses[29]. Additionally, the harsh conditions require

the use of precious metals throughout the whole device, which drastically increases costs. All of these factors reduce the economic viability of PEMWE devices as a route to green hydrogen production, and so current research must aim to address this.

### 1.2.3. Anion Exchange Membrane Water Electrolysis

By blending AWE and PEMWE, anion exchange membrane water electrolysis was recently developed to tackle the pitfalls of both pre-existing technologies. It operates under the same basic principles as AWE, with water being split to form hydrogen at the cathode, releasing hydroxide charge carriers which migrate to the anode to form oxygen. The crucial difference between AEMWE and AWE is that in place of the thick diaphragm, a thin membrane similar to that found in PEMWE is used – however it is now permeable to anions, not cations[31].

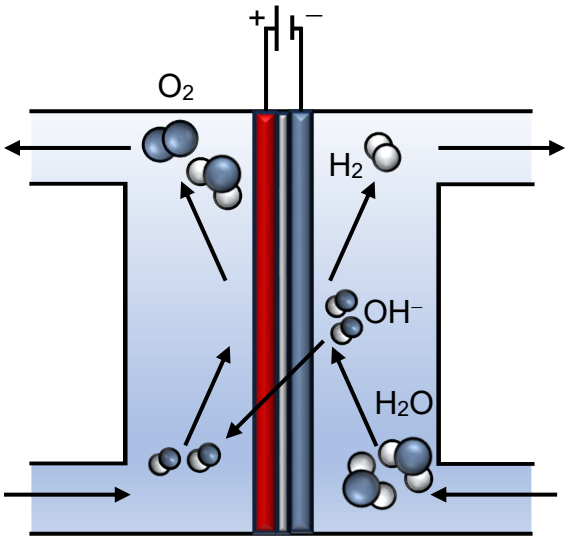


**Figure 6** – *Diagram showing the workings of an AEM water electrolyser. Water is split at the cathode (blue) to form hydroxide ions and hydrogen gas. The anions then permeate through the membrane to the anode (red) where they reform as water and oxygen gas. Electrons flow through the circuit to complete the process.*

A weakly alkaline solution or pure water is used to deliver reactants at temperatures comparable to AWE and PEMWE. Cathode catalysts include nickel and its alloys, while at the anode various combinations of nickel, iron and cobalt are used[31].

The use of alkaline media means non-precious metals are used throughout the cell, which significantly decreases the initial capital cost of the device. AEMWE devices carry several benefits of PEMWE - such as compact devices, rapid response times and high hydrogen purity (*ca* 99.99%)[31]. Additionally, the membranes used are composed of hydrocarbons – as opposed to the PFSA polymers used in PEMWE – meaning that there are notably less issues associated with their production[32].

Despite the many advantages of AEMWE, the technology is still developing and is not ready for commercial application. Devices operate at relatively low current densities (0.2-1 A $cm^{-2}$), caused by the sluggish HER - which is 3 magnitudes slower in alkaline media compared to acidic. While the small device size is beneficial in most cases, when paired with the low current density this advantage is neutralised. Further to this, the hydrocarbon membranes used are less stable than their PFSA counterparts, leading to devices with reduced lifetimes[32,33].

AEMWE has the potential to overcome the drawbacks faced by both AWE and PEMWE, however, the challenges stated above must be adequately addressed before wide-spread application can be considered.

Table 1 summarises the aforementioned three water electrolysis technologies.

| Parameter | AWE | PEMWE | AEMWE |
|---|---|---|---|
| **Charge Carrier** | $OH^-$ | $H^+$ | $OH^-$ |
| **Electrolyte** | 30 % KOH | Solid polymer | Solid polymer |
| **Anode Catalyst** | Ni oxides | $IrO_2$ | Ni/Fe/Co |
| **Cathode Catalyst** | Ni | Pt | Ni |
| **Bipolar Plates** | Stainless Steel | Ti | Stainless Steel |
| **Temperature (°C)** | 50-80 | 70-90 | 70-90 |
| **Pressure (bar)** | 2-10 | 15-30 | < 30 |
| **Current Density ($A\ cm^{-2}$)** | 0.2-0.4 | 1-2 | 0.2-1.0 |
| **Nominal Voltage (V)** | 1.8-2.4 | 1.8-2.2 | 1.8-2.2 |
| **Efficiency** | 70 % | 70 % | 70 % |
| **Lifetime** | 100,000 hours | 40,000 hours | 35,000 hours |
| **Hydrogen Purity** | 99.9% | 99.999% | 99.99% |
| **Advantages** | Established<br>Cheap hardware | High current density<br>Fast response time | Small device size<br>Cheap hardware |
| **Disadvantages** | Low current density<br>Large devices | Expensive<br>Supply chain issues | Low current density<br>Short lifetimes |

**Table 1** – *Table summarising three types of low temperature water electrolysis*[25,27,34–37].

Each water electrolysis technology has distinct advantages and disadvantages, however PEMWE and AEMWE are the most suitable candidates for green hydrogen production due to fast dynamic response times. The higher level of development in PEMWE means it is expected to become the dominant route to green hydrogen in the coming years, and so further research is required to ready the technology for wide-spread application.

## 1.3. Key Materials for Proton Exchange Membrane Water Electrolysis

A typical PEMWE flow cell is summarised in Figure 7. Each cell is composed of two end plates, two insulating plates, two bipolar plates and two gaskets which lie on either side of the

membrane electrode assembly (MEA)[36]. The end plates provide mechanical stability and allow for compression of the cell. Next there are insulating plates - commonly made of PTFE – which act as insulators to the electrical circuit, ensuring safety. The electrical charge is delivered through the bipolar plates which are in direct contact with the MEA, and gaskets are used on either side to prevent leakage.

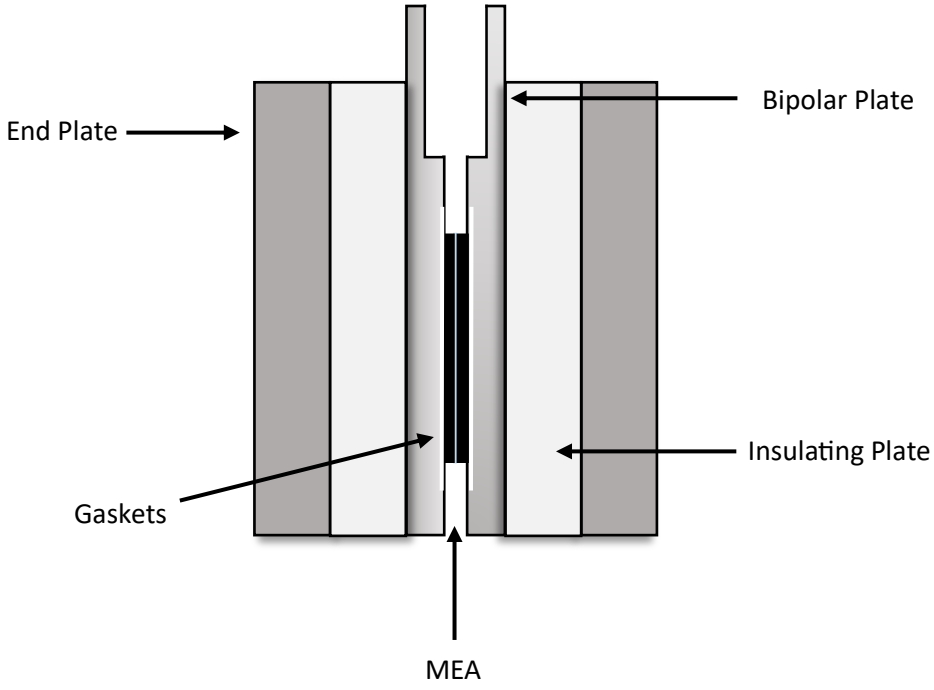


**Figure 7** – *Figure showing a schematic of a simple PEMWE cell. A MEA is sandwiched by a gasket, bipolar plate, insulating plate and an end plate on each side.*

Due to the extremely harsh environment found within the cell, titanium bipolar plates must be used which constitute around 50% of the initial cell cost[38]. Cheaper materials such as carbon graphite have been tested, however the plates were found to oxidise and corrode in extended durability tests[39]. To preserve the lifespan of titanium plates they are often coated in an anti-corrosion layer.

In practice, many PEMWE devices operate as a stack of cells. This is when multiple cells are combined within a larger device to reach higher outputs. An example of a working industrial PEMWE stack is shown in Figure 8[40].

**Figure 8** – *Image of three industrial PEMWE stacks. Product of Siemens Energy*[40].

### 1.3.1. Membrane Electrode Assembly

The MEA is the heart of the cell, consisting of two electrodes – the anode and cathode – and a PEM which separates them. Within each electrode, there are three distinct layers:

1. The Gas Diffusion Layer (GDL) – This is the outermost layer of the electrode, and it provides structural support while also facilitating the movement of reactants/products.
2. The Microporous Layer (MPL) – The role of this layer is to enhance the transport of reactants and prevent flooding of catalyst surface sites.
3. The Catalyst Layer (CL) – The catalyst layer is responsible for carrying out the desired reaction and is in direct contact with the PEM.

These layers are visualised in Figure 9.

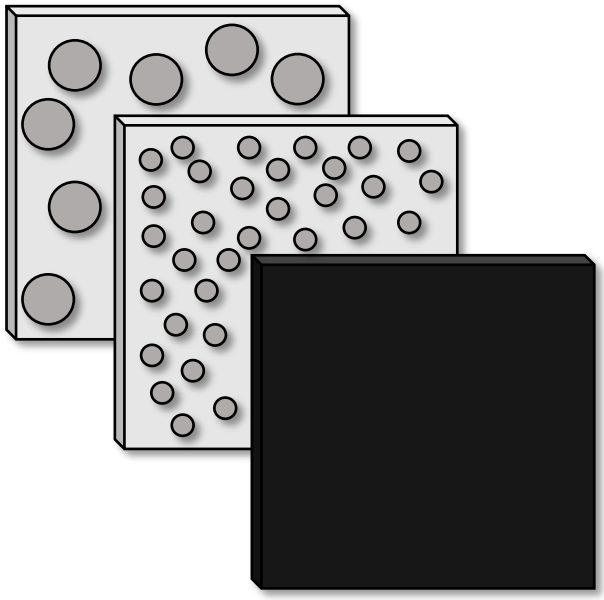

**Figure 9** – *Schematic showing the different layers of the electrode. From back to front: the GDL with large internal pores, the MPL with small internal pores, and the uniformly distributed CL. Sizes of pores exaggerated for understanding.*

#### 1.3.1.1. Gas Diffusion Layer

The gas diffusion layer provides a support for the MPL and CL, however it also serves a range of roles that are crucial to the cell's function. An effective GDL must[41]:

- Deliver electrons to the bipolar plates
- Control the influx of water molecules to the MEA
- Control the outflux of product gases away from the MEA
- Protect the catalyst layer from mechanical damage

Through a complex network of pores, the GDL optimises catalytic activity by ensuring reactants are evenly distributed across the surface of the electrode[42]. This hydrates the PEM to maintain optimum performance, whilst also fighting against over saturation. If the system was over saturated, local pressure hot spots could form on the CL thus destroying its structural integrity. In some instances, the GDL is coated with a hydrophobic substance (such as PTFE) which further aids in surface flooding prevention, however this will increase cell resistance so should be employed with caution[43].

At the cathode, the GDL is made of porous carbon cloth - an extremely strong and lightweight material utilised in many different industries. It is very conductive and pore size can be modulated during fabrication, meaning that product/reactant diffusivity can be controlled depending on the specific requirements of the cell.

Porous titanium materials such as fibre felt or mesh are used as anode GDLs, owed to their excellent corrosion resistance. This comes from the material's ability to form a thin layer of oxide film on the surface upon exposure to air which protects the underlying metal[44]. Pore diameter is typically in the low tens of microns range and the optimum porosity for a GDL is 50 %[36]. Unfortunately, current titanium fibre felt/mesh manufacture cannot regulate pore size, which results in inhomogeneity across samples[37]. Additionally, the high capital cost and poor conductivity of titanium create further limitations with its use.

Challenges in GDL research are related to the many functions required of a successful GDL, as optimisation of one parameter often leads to the decrease in performance of another[45]. For example, increasing pore size boosts gas diffusion but decreases mechanical strength, and adding a thicker hydrophobic coating prevents flooding but increases internal resistance. Moreover, there has been a notable lack of research on GDL performance compared to other MEA components such as electrocatalysts and PEMs. This may be due to the challenges associated with studying the molecular diffusion through the GDL[46]. This would require the solid surface, liquid reactant and gaseous products to be analysed in situ, which would be very challenging in a conventional electrochemistry laboratory.

#### 1.3.1.2. Microporous Layer

The microporous layer lies between the GDL and CL, where it acts to provide a seamless transition between the two sections[47]. It will often be composed of a similar material to the GDL - for example, at the anode the MPL is commonly made of Ti nanoparticles. At the molecular level the catalyst surface is not uniformly smooth, so when the electrolyser is assembled there are gaps between the CL and the rest of the electrode. The addition of an MPL bridges these sections, thus reducing the interface contact resistance of the system[36].

Upon MPL addition, the surface pore size is reduced which boosts to the desired mass transport of the electrolyser. A study by Deng *et al* in 2023 found that upon by adding a MPL on to the

GDL, the average pore diameter on the surface decreased by 29.7 %. This is shown by the scanning electron microscope (SEM) images in Figure 10[48].

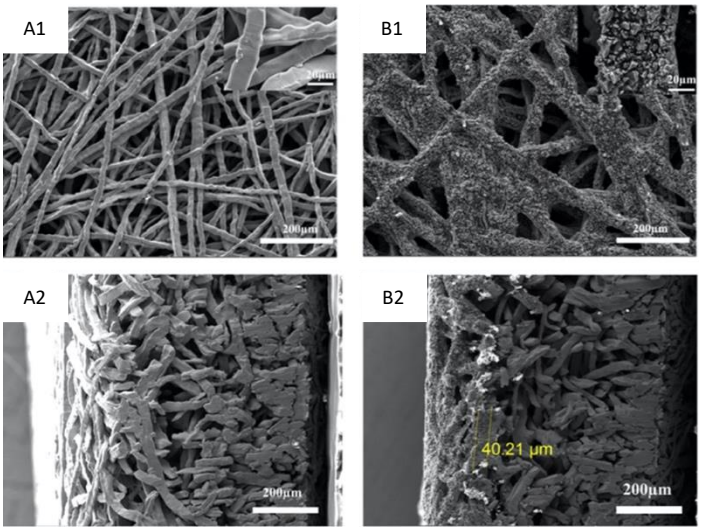


**Figure 10** – *Images A1 and B1 show the surface SEM images of raw titanium fibre felt and titanium fibre felt coated with titanium microparticles (1-5 µm in diameter), respectively. Images A2 and B2 show a SEM image of the cross-section of the same samples*[48].

The experiment produced an electrode with large internal pores (close to the GDL) and small pores on the surface (close to the CL). This is advantageous as larger pores favour mass transport of liquid reactants and the smaller pores direct product gases away from the catalyst layer – thus exposing the catalyst surface to more reactants[49]. The reduced surface pore size also prevents the CL penetrating deep into the GDL. Similar to the increased contact between the GDL and the catalyst, this increases catalytic contact with the membrane – further reducing the interface contact resistance and boosting device performance[47].

The exact mechanisms of MPL function are hard to elucidate for similar reasons to that when studying the GDL[46]. This presents a challenging but worthwhile research avenue, as fine tuning the central layer of the electrode will aid in the optimisation of device performance.

#### 1.3.1.3. Catalyst Layer

The catalyst layer is made of three components – the catalyst, a dispersion agent (to prevent catalyst aggregation) and an ionomer (to increase conductivity). From here, two configurations are commonly used to produce the CL – the catalyst-coated substrate (CCS) and the catalyst-

coated membrane (CCM)[50]. In the CCS, the catalysts are applied directly onto two different electrodes which are then separated by the membrane, whereas in the CCM both the OER and HER catalysts are coated directly onto opposite sides of the same membrane. This is shown in Figure 11.

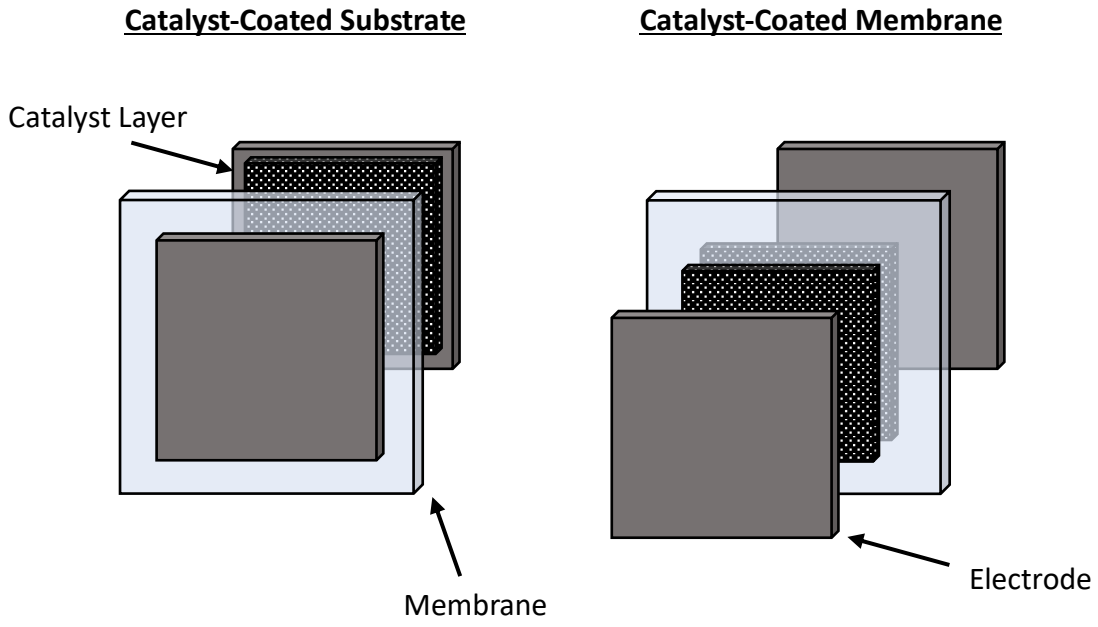


**Figure 11** – *Schematic of the two different catalyst configurations. On the left, the CCS is shown. On the right, the CCM is shown.*

The CCM is produced through either the direct spraying of a catalyst ink on to the membrane or by depositing a catalyst ink on to an intermediate material, which is then hot pressed onto the membrane. This is the traditional method that was first employed by General Electric in the 60's and is still popular today[51]. This method is favoured for providing close contact between the CL and the membrane, which reduces the interface contact resistance thus optimising catalyst activity. However, challenges with complex production methods and membrane swelling causing catalyst detachment led to the development of the simpler CCS method.

The CCS technique is popular because of the simple fabrication process, which has allowed successful scale-up to industrial level. Compared to the CCM, this method has lower catalytic utilisation as there is less membrane – catalyst contact, however an MPL can combat this[47,52]. The CCS approach means the CL is unaffected by fluctuations in membrane morphology and

also enhances electrical conductivity. It has also been shown that at the current densities used in commercial PEM water electrolysers, the CCS systems outperform those with CCMs[50].

Each fabrication method has specific advantages and areas for improvement. It is ultimately at the discretion of the user to decide which configuration suits application best. The accessibility of CCS makes it an obvious choice for inexperienced users, however the CCM may be more useful when trying to optimise catalyst utilisation.

## 1.4. Proton Exchange Membranes

### 1.4.1. Fundamentals

The proton exchange membrane is responsible for transporting protons produced at the anode to the cathode where hydrogen gas is produced. Efficient membranes must[53]:

1. Be highly conductive towards protons
2. Be highly insulating towards electrons
3. Have excellent thermal, mechanical and electrochemical stability
4. Have very low product permeability
5. Be viable from a cost and durability perspective

Commercial proton exchange membranes are mostly made of PFSA, with DuPont being the first to successfully synthesise and sell these membranes under the Nafion™ brand in the 60's[54]. Since then, Nafion™ has remained as the leading membrane, however other brands such as Aquivion® by Solvay are now available. The membranes function in the hydrated state and range in thickness between 100-180 μm. When selecting a membrane, care should be taken to balance the performance trade-offs, as thinner membranes report higher activity but lower mechanical strength[37]. As a result, thinner membranes are more likely to degrade and display higher rates of unwanted gas crossover. The basic structure of a PFSA based membrane is shown in Figure 12.

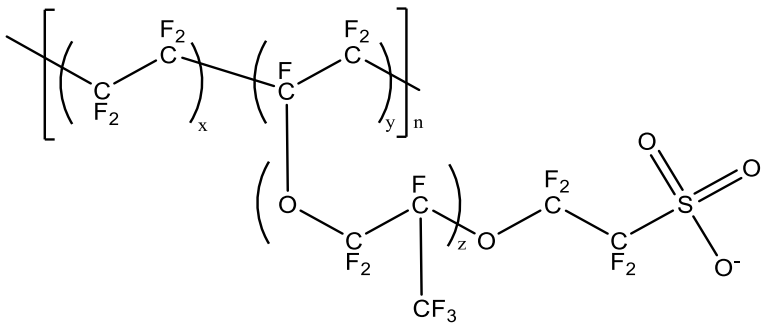

**Figure 12** - *Chemdraw drawing showing the basic molecular structure of a PFSA based membrane. The polymers have a long PTFE-like backbone with side chains made of perfluorinated vinyl ethers capped by perfluorosulfonic acid end groups.*

The main variation amongst PFSA PEMs is the length of the side chain, Z. For example, in Nafion™ Z = 1, and so it is classed as a long side chain membrane, whereas in Aquivion® Z = 0, thus classifying it as a short side chain membrane[55]. While the effects of varying membrane side chain lengths are widely reported for PEM fuel cells, there is limited data studying the effect in water electrolysers[56–58]. These fuel cell studies are not directly applicable due to different operating conditions; however, they suggest short side chain membranes to perform superiorly.

At present, there is one study in the literature investigating the effects of a short side chain membrane vs a long side chain membrane in PEMWE. The researchers used a range of electrochemical and characterisation techniques to thoroughly evaluate each membranes performance[59]. In all areas tested, the short side chain membrane was shown to outperform the long side chain membrane, and the authors concluded this to be a result of the effects of varying side chain length on the membranes structural properties. Unfortunately, the study failed to compare the two membranes on stability, which is one of the most crucial factors when assessing PEMs. This data shows that short side chain membranes demonstrate superior performance in PEMWE, however further studies are needed to support this. By better understanding the effects of polymer morphology on device performance, it will allow for more informed decisions when selecting the membrane for use.

Due to trademarking, literature on the exact synthetic and production methods of the branded membranes are limited, however it is thought that they are formed by free radical copolymerisation[53]. This creates a multifunctional polymer with two discrete regions.

The first region is the hydrophobic PTFE backbone which provides thermal, mechanical and electrochemical stability due to the strong carbon – fluorine bond[60]. The second region of the membrane is formed by the hydrophilic sulfonic acid side chains. Due to the different polarities, separation naturally occurs giving rise to hydrophilic channels within the membrane. These channels allow for water absorption into the membrane and are referred to as cluster phase domains. Nano-sized channels link these domains and ensure the membrane is evenly saturated with water[61]. A simplified schematic of a PEM in the hydrated state is provided in Figure 13.

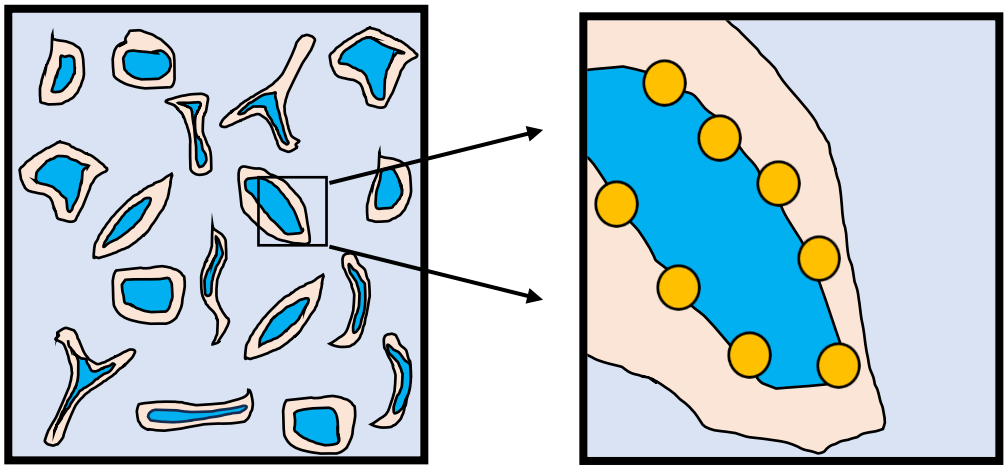

**Figure 13 -** *Simplified diagram of the discrete areas of a PFSA membrane in the hydrated state. The lilac area represents the hydrophobic PTFE backbone, the beige areas represent the hydrophilic cluster phase network, the orange circles represent the sulfonic end groups, and the blue area represents absorbed water.*

Proton conduction across the membrane occurs via the following three mechanisms[62]:

1. Surface hoping – Protons hop across the membrane by making and breaking hydrogen bonds with the charged sulfonic groups that cap the side chains.
2. The Grotthus Mechanism – Protons hop across the membrane by making and breaking hydrogen bonds with absorbed water molecules.
3. The Vehicular Transport Mechanism – Protons transfer through the membrane attached to a carrier, for example the hydronium ion ($H_3O^+$). The voltage applied across the cell causes the charged ions to migrate across the membrane, subsequently releasing one proton and one molecule of water. This is linked to the electroosmotic drag phenomenon observed in many electrolysis devices.

Which mechanism is dominant depends on a variety of factors - like water content in the membrane or diffusion coefficients, however it is widely accepted that all three mechanisms are present in most electrolysers[63].

### 1.4.2. Challenges

Due to the integral role the PEM plays within the system it is crucial that they maintain structural integrity under operation. Unfortunately, membranes have the shortest lifetime of all cell components and degradation is one of the most common causes of device failure[64]. Membranes can degrade by any of the following mechanisms:

1) Mechanical instability: The membrane experiences mechanical wear and tear
2) Thermal instability: The membrane degrades due to high temperatures
3) Chemical instability: When the harsh oxidative conditions cause the surface to react

The result of this degradation is membrane thinning and pinhole formation on the surface, which increases the rate of unwanted hydrogen crossover at the anode. This not only creates an explosive gas mixture, but also harmful oxidising agents like hydrogen peroxide or free radicals at the catalyst-membrane interface. These compounds react to 'unzip' the membrane, which increases the rate of gas crossover further and repeats the cycle[65]. From here, device efficiency gradually drops through a variety of routes such as catalyst leaching, reduced active membrane area or increased internal temperature[66].

Grigoriev et al tested Nafion™ in a MEA using load cycling for 5500 hours, after which the system experienced a short circuit and shut down[67]. The team conducted post-mortem analysis to determine the cause of breakdown, and a transmission electron microscopy image of the membrane is shown in Figure 14.

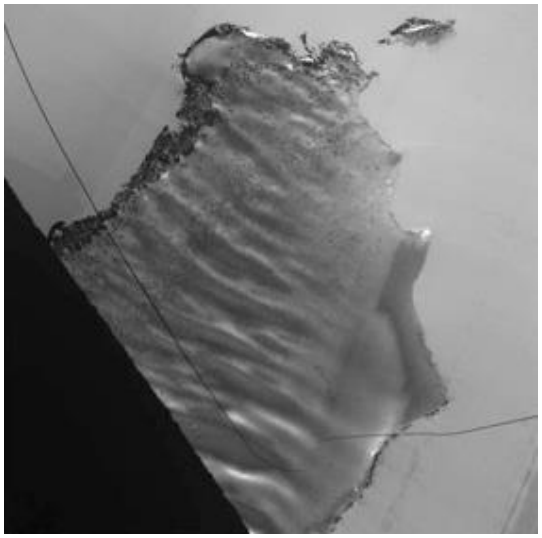

**Figure 14** – *A transmission electron microscopy image at low magnification of Nafion™ 115 after 5500 hours operation. The central area of the image shows an area of the membrane that has been physically damaged*[67].

Figure 14 shows a section of the membrane that has undergone a morphological change over the duration of the experiment. Further analysis revealed that the observed change was membrane thinning, and on average the surface thickness had decreased by 75 %. The team believe this is what ultimately caused cell failure. A thicker membrane could increase device lifetime, however this would reduce device performance due to higher resistance.

The advantages of performing water electrolysis at elevated temperatures have been previously discussed, however the PEM limits operating conditions to 80 °C. At temperatures above 80 °C, most PFSA based membranes start to degrade. If membranes with greater thermal stability were developed, high pressures or an anhydrous proton carrier such as phosphoric acid could be used to allow proton conduction at elevated temperatures, thus reducing the electrical energy requirement of the cell[68].

There are also many challenges that lie in the production of PFSA membranes due to the use of highly dangerous and expensive monomers[69]. PFSA materials are carcinogenic 'forever chemicals' meaning they persist within living organisms for extended time periods and have been proven to cause cancer in humans[70]. Because of these complications, the number of companies willing to produce PFSA based membranes is limited.

Supply issues have plagued the industry for years and recently the two most popular membranes – Nafion™ and Aquivion® - have been discontinued by leading suppliers. The reasoning for this remains unclear, however it is thought to be down to previously stated production issues. The discontinuation of these products has caused existing stock prices to skyrocket and cast great uncertainty over the future of the technology. If there is no PEM, there is no PEMWE and so finding an alternative available membrane delivering on performance and stability is one of the most crucial challenges facing the industry at present.

### 1.4.3. Alternative Membranes

Current research is exploring the use of non-PFSA based membranes and hydrocarbon membranes may be a possible solution[71]. Bulky aromatic heterocycles in the polymer backbone can provide thermal stability and sulfonic groups on side chains can provide the necessary proton conductivity. The monomers are also cheap, available commercially and have heterocyclic groups susceptible to electrophilic or nucleophilic attack – presenting a potential route for simple structural modification to create desired characteristics[60,72].

The use of hydrocarbon based membranes for PEMWE devices has been scarcely reported in the literature, as performance of existing PFSA based membranes was historically deemed sufficient[73]. Nevertheless, in 2020 Klose et al compared a sulfonated poly phenylene sulfone (sPPS) PEM against Nafion™ in PEMWE. The molecular structure is shown in Figure 15[74].

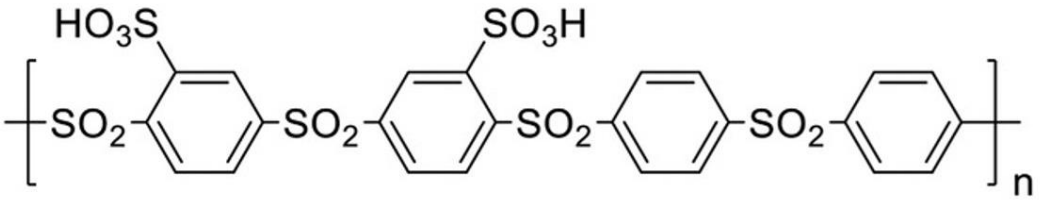


**Figure 15** – *Molecular structure of the sPPS PEM used in the study*[74]

The team tested the sPPS membrane against Nafion™ 115 in a MEA to compare the effects on electrolyser operation. It was found that the sPPS-MEA delivered outstanding performance in linear sweep voltammetry (LSV) tests – operating at 3.5 A $cm^{-2}$ at 1.8 V, compared with the Nafion™-MEA which only reached 1.5 A $cm^{-2}$ at the same voltage. Hydrogen crossover at the anode was also investigated, and the sPPS-MEA showed three times less crossover than the

Nafion™-MEA. The reduced gas crossover in hydrocarbon membranes is discussed in the literature[75,76]. This is thought to be explained by the lack of side chains in hydrocarbon membranes, meaning there is reduced free volume for hydrogen gas to pass through when compared to PFSA based membranes[77].

As hydrogen crossover is known to directly decrease device performance, it could be hypothesised that the sPPS-MEA would be more stable than the Nafion™. However, in a 100 hour stability test Nafion™ performed notably better than two sPPS samples (Figure 16).

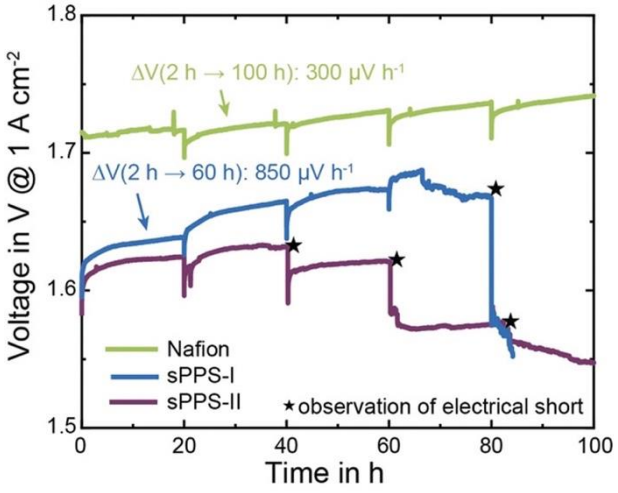


**Figure 16** – *Chronopotentiometry experiment at 1 A cm$^{-2}$ over 100 hours. Three different MEAs were tested. One contained Nafion™ 115 as the PEM (green) while the remaining two utilised sPPS (green and purple). Black stars represent an electrical short circuit*[74].

The MEA using Nafion™ was found to have a degradation rate of 300 μV h$^{-1}$, which is less than the rate reported for sPPS-I (850 μV h$^{-1}$). Additionally, the MEA containing Nafion™ showed steady degradation over the full test, whereas sPPS-I degradation started to waver after around 60 hours. No degradation rate was reported for sPPS-II as the system experienced multiple short circuits. The authors reported that the short circuits were caused by the membrane. The higher stability of Nafion™ is assigned to the strong carbon-fluorine bond within the backbone, which increases resistance to degradation mechanisms.

Free radicals are known to be a key contributor to membrane degradation and so to increase the durability of hydrocarbon membranes, one paper reported the use of a radical scavenger

interlocking interfacial layer[78]. By creating a complex cerium oxide radical scavenger and applying a thin Nafion™ coating, a hydrocarbon membrane was reported to operate with increased stability. While the technique did significantly improve the stability of the hydrocarbon membrane, it ultimately relied on the use of a PFSA material to reduce the degradation rate.

By 2030, hydrocarbons are expected to become the material of choice for PEMs, - however given the recent discontinuation of the most popular PFSA based membranes, this is not sufficient to meet the current demands of research[79]. At present, there is no access to a reputable, available PEM and this issue must be resolved soon in order to reduce the impact on PEMWE research.

## 1.5. Hydrogen Evolution Reaction

### 1.5.1. Fundamentals

The hydrogen evolution reaction occurs at the cathode and can follow one of two mechanisms[80,81]. The first is the Volmer-Tafel, which proceeds by the following two steps:

$$Volmer\ step - H^+ + e^- \rightarrow H_{(ads)}$$
$$Tafel\ step - 2\,H_{(ads)} \rightarrow H_2$$

In the Volmer step, one proton is adsorbed on to the surface of the catalyst site, forming an intermediate represented by $H_{(ads)}$. Next, the Tafel step takes places where two equivalents of this intermediate are combined to form diatomic hydrogen.

The second reaction mechanism is known as the Volmer-Heyrovsky process, which also starts with the Volmer step. Diatomic hydrogen is then formed through the Heyrovsky step, where an adsorbed proton intermediate ($H_{(ads)}$) reacts with one proton and one electron. This is represented in the equation below.

$$Heyrovsky\ step - H_{(ads)} + H^+ + e^- \rightarrow H_2$$

In both mechanisms the adsorbed proton intermediate is involved in each step so its binding energy to the catalyst surface plays a crucial role in mediating the rate of reaction. If the Gibbs

free energy of adsorption ($\Delta G_{H(ads)}$) is too high, then adsorption will be unlikely to occur and so the Volmer step will limit the reaction. Alternatively, if $\Delta G_{H(ads)}$ is too low then the adsorbed intermediates will bind too strongly, thus inhibiting the Tafel or Heyrovsky step[82]. This is an example of Sabatier's principle which states that catalyst-reactant interactions should be 'just right' – meaning that binding should not be too weak or too strong in order to perform optimally[83]. These binding energies ultimately control the HER rate and catalyst performance.

### 1.5.2. Hydrogen Evolution Electrocatalysts

The most active HER catalysts are noble metals – namely platinum, but also rhenium, ruthenium and iridium. These metals optimise the ideal $\Delta G_{H(ads)}$ value for the HER reaction and the volcano plot in Figure 17 compares the performance of other common catalysts[81].

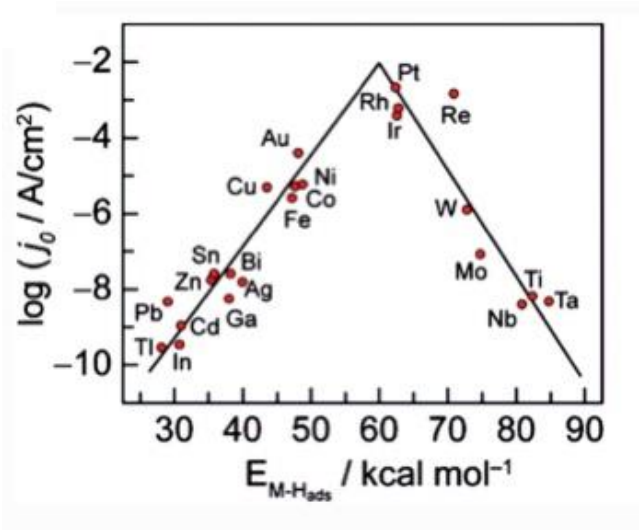


**Figure 17** - *Volcano plot showing the energy of the catalyst surface site – H bond against exchange current density for common metal catalysts in acidic media, as found in PEMWE*[81].

State of the art electrolysers use platinum on carbon cathodes with a loading mass *ca* 0.5 mg $cm^{-2}$ and around 40 % weight platinum[37]. Platinum has surface sites with optimum binding energies so demonstrates excellent activity, and also has high corrosion resistance which gives rise to long term stability under the harsh acidic conditions. However, platinum is one of rarest metals in the earth's crust and as a result is very costly. While the element is commonly used as a catalyst in many other industries, the implementation of a large scale PEMWE industry would strain current supplies and potentially lead to a resource bottleneck[39,84]. In order to

prevent this and drive electrolyser costs down, researchers are seeking methods to reduce the platinum loading mass in the catalyst. This is being done by developing noble metal free catalysts, creating alloys and reducing catalyst particle size[85–87].

That said, relative to the catalysts used at anode side, platinum reserves are significantly higher and the cost per gram is notably less. Moreover, the kinetics of the HER are extremely fast compared to the sluggish OER[88]. This means the cathode reaction has a lower overpotential and explains why platinum loading mass can be reduced significantly without impeding electrolyser performance[89]. While reducing platinum content is undoubtedly important to reduce costs, many researchers believe that optimisation of the OER catalyst - in terms of costs *and* performance - is a more pressing issue.

## 1.6. Oxygen Evolution Reaction

### 1.6.1. Fundamentals

The OER is a slow process occurring at the anode, requiring large over potentials to drive the reaction to completion. Due to the longstanding presence of AWE, historically mechanistic OER studies focused on alkaline media. This meant that the bulk of studies in acidic media were theory based and used density function calculations to derive mechanisms – which led to the discovery of the adsorbate evolution mechanism[90].

In this mechanism, one molecule of water is adsorbed on to an active site, where it immediately undergoes two successive deprotonation steps. An electron is also released alongside each proton. This leaves an adsorbed oxygen intermediate on the catalyst surface that undergoes nucleophilic attack by another molecule of water. The result is a new oxygen – oxygen bond, in addition to the release of another proton and electron. The oxygen intermediate then undergoes a final deprotonation (paired with the loss of an electron), and diatomic oxygen is released from the surface[91]. The following equations describe this process where (ads) represents an adsorbed species[92,93].

$$H_2O\ (l) \rightarrow OH_{(ads)} + H^+ + e^-$$

$$OH_{(ads)} \rightarrow O_{(ads)} + H^+ + e^-$$

$$O_{(ads)} + H_2O \rightarrow HO_{2(ads)} + H^+ + e^-$$

$$HO_{2(ads)} \rightarrow O_2\ (g) + H^+ + e^-$$

The recent rise in popularity of PEMWE has increased the number of lab-based mechanistic studies, and a new mechanism has been proposed to work alongside the adsorbate evolution mechanism. Through the isotopic labelling of oxygen atoms, it was found that lattice oxygen plays a role in the OER – in what is now known as the lattice oxygen mechanism[94,95].

The mechanism proceeds by the same first two successive deprotonation steps observed in the adsorbate evolution mechanism. From here, an oxygen present in the catalyst lattice combines with the adsorbed oxygen intermediate to form diatomic oxygen, leaving an open oxygen vacancy in the extended structure of the catalyst. A water molecule then occupies this site, which is deprotonated to leave one adsorbed hydrogen on the surface. This adsorbed hydrogen is then released thus restoring the catalyst surface[81]. This is summarised below, where $O_l$ represents lattice oxygen, and $V_o$ represents an oxygen vacancy[96].

$$H_2O\ (l) \rightarrow OH_{(ads)} + H^+ + e^-$$
$$OH_{(ads)} \rightarrow O_{(ads)} + H^+ + e^-$$
$$O_{(ads)} + O_l + \rightarrow O_2(g) + V_O$$
$$V_O + H_2O\ (l) \rightarrow O_l + H_{(ads)} + H^+ + e^-$$
$$H_{(ads)} \rightarrow H^+ + e^-$$

In any given system both mechanisms are present, however the dominant process will depend on specific reaction conditions. For example, the absorbate evolution mechanism is most active at low voltages, while at high voltages the lattice oxygen mechanism is thought to dominate[97]. Additionally, the lattice based mechanism is highly dependent on surface structure, meaning that any surface degradation will cause the OER rate to decrease rapidly. By fully understanding each reaction mechanism, research can be better informed as to the best routes to optimise catalytic performance.

### 1.6.2. Oxygen Evolution Electrocatalysts

As previously stated, due to the harsh acidic environment and high energy demand of the OER, only the most inert and catalytically active materials can be used as electrocatalysts[98]. Additionally, Sabatier's principle means that the catalyst will have to bind optimally to the four different adsorbed intermediates involved across the two OER mechanisms – which means

very few catalysts are suitable for the reaction[37]. Figure 18 compares different catalyst groups for performance in the OER in acidic media[91].

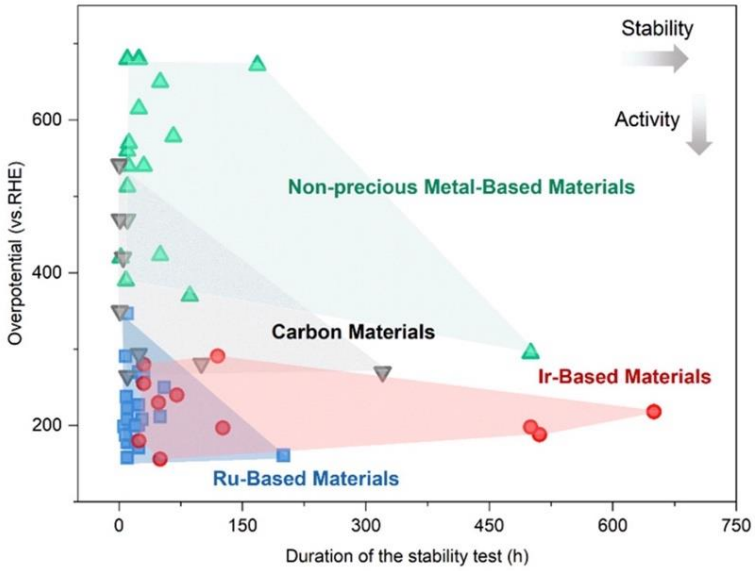


**Figure 18** – *Figure comparing the results reported in the literature from four different classes of catalyst in terms of length of stability test (hours) and overpotential (mV). The four classes are iridium-based materials (red), ruthenium-based materials (blue), carbon materials (grey) and non-precious metal-based materials (green). A higher length of stability test indicates a more stable catalyst, and a lower overpotential indicates a more active catalyst* [91].

From Figure 18, it can be seen that the materials with the highest activity are generally those containing iridium or ruthenium. Despite generally having a higher activity towards the reaction, the use of ruthenium is precluded in real devices due to the formation of soluble ruthenium oxides, which leads to rapid corrosion of the catalyst[99]. Iridium oxide is viewed as the 'state-of-the-art' catalyst due to its exceptional stability, with commercial devices operating at a loading mass *ca* 2 mg $cm^{-2}$. Unfortunately, iridium is also one of the rarest metals on earth, and only around 7 tonnes are produced per annum[100]. It has been proposed that if current iridium production rates are to match the predicted demand of PEMWE technology, the loading mass within devices should be cut drastically to between 0.05 – 0.10 mg $cm^{-2}$ [29].

Although iridium is the most stable known catalyst for the OER in acidic media, it still degrades before most other cell components. Each specific catalyst will have an exact degradation route, however they typically break down due to agglomeration, oxidation or dissolution[37].

Agglomeration of catalyst nanoparticles decreases activity by reducing the number of available surface sites. At potentials greater than 1.8 V, iridium dioxide will gradually oxidise to produce unstable $IrO_x$ compounds on account of the increased lattice oxygen mechanism[101]. Over time, this changes the structure of the catalyst surface from crystalline to amorphous, thus increasing the susceptibility to corrosion and dissolution.

Current research aims to tackle these challenges by reducing iridium loading mass while also maintaining stability. As with HER catalysts, this is being done through the development of noble metal free catalysts, alloys and the reduction of catalyst particle size down to the single atom level[102].

The literature is rich with novel OER catalysts - boasting low iridium content and activities several magnitudes higher than benchmark iridium dioxide, however the biggest challenge lies in producing a catalyst with sufficient stability[103–105]. Non-noble metals and alloys have been shown to demonstrate sufficient catalytic activity, yet their reports often lack stability data – likely due to the use of non-corrosion resistant materials. Should the issues surrounding the incorporation of single atom catalysts into the MEA be solved, a 'gold-standard' OER catalyst may be developed in the future.

## 1.7. Challenges within Proton Exchange Membrane Water Electrolysis Research

When evaluating the factors inhibiting PEMWE from dominating the global hydrogen market, it appears the two biggest issues are weak proton exchange membranes and costly OER catalysts. The further optimisation of these components will reap many rewards such as longer device lifetimes, increased performance and reduced cost. Unfortunately, their development is hindered by a lack of structure across research within the field.

### 1.7.1. Calls for Standardisation

It is widely recognised that a standard testing procedure for novel PEMWE components is urgently required to create a cohesive research field that works together towards solutions[106]. Unlike PEM fuel cells (which have received significant research, industry, and government influence in terms of standardising testing procedures[107–109]), PEMWE research has historically received little influence from governing bodies. This has led to a lack of consistency across research in terms of testing equipment, operating parameters and results reporting which has slowed the development of the technology.

This was recognised in 2021 by the EU commission (alongside their industrial and research partners), who aimed to resolve these issues by publishing guidelines for testing low temperature water electrolysers[110]. Unfortunately, the guidelines have not been widely adopted within the community, as highlighted in a recent review by Tomic *et al*[111]. The authors placed this on account of electrolysers being extremely complex multi-component systems, and the equipment recommended for testing being uncommon in most labs. Additionally, the work did little to standardise testing of individual components, as it referred to whole devices throughout. If standard procedures for testing things like novel catalysts or membranes were available, PEMWE development would be propelled forward in a bottom-up approach.

For example, when testing novel catalysts two different systems are commonly used – the rotating disk electrode or the MEA. Each method is chosen for a particular reason based on the research needs, however they operate under very different conditions which alter the catalytic activity and so these results cannot be compared[112]. A comparison of the two different techniques is given in Table 2[113].

| Parameter | Rotating Disk Electrode | MEA |
|---|---|---|
| **Catalyst Mass Required** | 1 – 10 mg | 0.2 – 2 g |
| **Experiment Duration** | Minutes to hours | Days to weeks |
| **Operating Temperature** | 10 – 80 °C | 40 – 95 °C |
| **Dominant Mass Transport Regime** | Liquid diffusion boundary layer | Gas phase diffusion |
| **Mass Transport-Limited Current Density** | 10 mA $cm^{-2}$ | > 4 A $cm^{-2}$ |
| **Maximum Specific Current Density** | 10 mA $cm^{-2}$ | 100 mA $cm^{-2}$ |

**Table 2** – *Table highlighting the main differences between rotating disk electrode and MEA systems*[113].

Across the field there is no set 'benchmark' OER catalyst that is consistently used as a reference when testing novel cell components. Within the literature, the 'commercial' catalyst layer used can vary greatly – from iridium powder to nanoparticles to adding a titanium support[114–116]. These changes will vary catalyst performance significantly, meaning that the true effects of a

novel component may not be fairly evaluated with reference to the literature. There are countless other parameters which vary across devices - such as membrane thickness or catalyst loading mass - and the effects of these compound to produce incomparable results across papers, reducing the efficiency of research.

Finally, stability tests of PEMWE devices are often run under potentio or galavanostatic conditions, which do not truly replicate the environment of working electrolyser coupled to renewable energy. It has been shown that fluctuating operating conditions cause significantly more degradation than static procedures, and so testing under these conditions is crucial when evaluating how devices perform in practice[65].

### 1.7.2. Need for a New Membrane

The complications involved in PEM production have most recently manifested as the discontinuation of the two most popular membranes – Aquivion® and Nafion™. This is a serious issue and the identification of a new membrane with similar (if not superior) performance parameters should be the focus of current research efforts. The development of a standard testing procedure or novel catalyst is futile if the key component of the electrolyser is missing.

Other commercial membranes are available - for example FuelCellStore (a leading electrolyser component retailer) stocks some unbranded alternatives. At the time of writing there is no data within the literature regarding the performance of these membranes, which casts doubt over their efficiency. These unbranded membranes must be urgently tested and compared against the branded counterparts, so that their use within research can be encouraged or opposed to allow for the continued development of PEM water electrolysers.

## 1.8 Research Outlook

At present, there is only one paper comparing short side chain and long side chain membrane performance in PEMWE[59]. More importantly, a successor to Nafion™ and Aquivion® has not yet been identified given their recent discontinuation. This work seeks to remedy these issues by investigating the effects of an unbranded membrane (D170-U, thickness 170 μm) on PEMWE device operation and comparing this against Aquivion® E95-1S (thickness 150 μm) and Nafion™ 117 (thickness 180 μm). The structures of each membrane are shown in Figure 19.

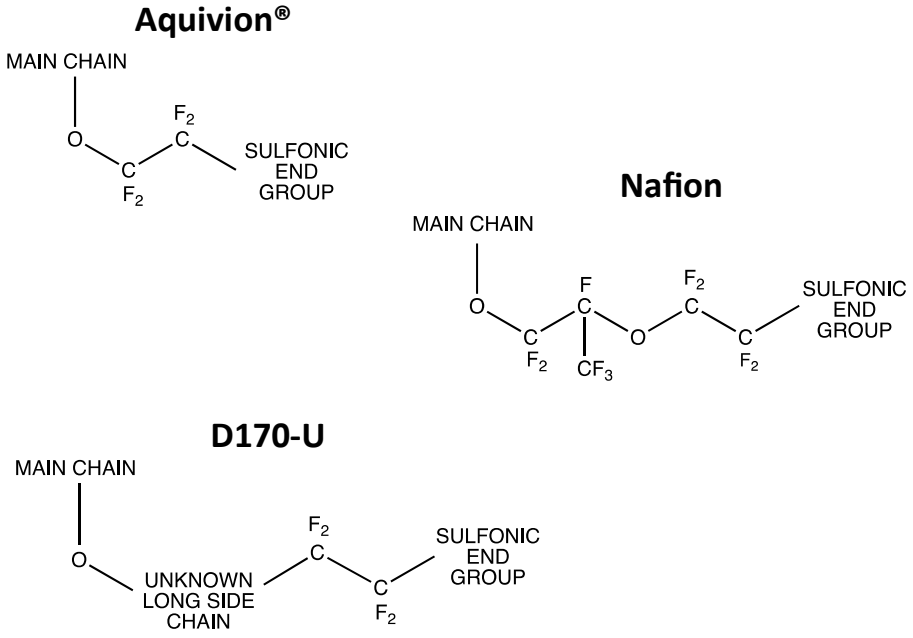


**Figure 19 –** *Chemdraw drawing showing the chemical structure of each membrane used in this study. The main chain is a PTFE-type backbone and the side chains are capped with a sulfonic ($SO_3^-$) unit. While the exact length of the side chain in D170-U remains unknown, the suppliers have stated it 'is the same or similar to Nafion™ 117'.*

By testing a short side chain membrane against two long side chain membranes, the effects of side chain length on electrolyser operation can be established. The testing of D170-U will provide information as to whether the membrane is suitable for application in PEMWE research.

## 1.9 Project Aims

The project aims to investigate the effects of using a short side chain membrane compared to a long side chain membrane on PEMWE device operation. It also aims to determine if a new, unbranded membrane has similar operating parameters to the two branded membranes, to determine if it is suitable for application in future PEMWE research. Three key parameters will be investigated - performance, degradation rate and hydrogen crossover at the anode after use. This will be done in a flow cell through LSV, electrical impedance spectroscopy (EIS), chronopotentiometry and gas chromatography. To understand the results gathered, post-mortem characterisation of the system will be conducted via SEM and inductively coupled plasma-optical emission spectroscopy (ICP-OES).

It is hypothesised that Aquivion® will demonstrate superior performance compared to the other two membranes due to reduced side chain length. Additionally, Aquivion® is expected to display a lower degradation rate and lower rate of hydrogen crossover after chronopotentiometry when compared to the other two membranes. When comparing Nafion™ and D170-U, it is hypothesised that due to the reduced thickness of D170-U, it will display higher performance but also a greater degradation rate and hydrogen crossover rate after chronopotentiometry testing than Nafion™.

# 2. Experimental Techniques

## 2.1. Electrochemical Techniques

The field of electrochemistry relies on a range of electrochemical techniques to assess performance and elucidate reaction mechanisms. This is done by measuring a system's response to a current or potential, and the techniques used in this study will herein be discussed.

### 2.1.1. Linear Sweep Voltammetry

Linear sweep voltammetry is one of the fundamental techniques used in electrochemical research and was first reported by Matheson and Nichols in 1938[117]. It is the primary means of testing PEMWE device performance, as it allows the rapid determination of current density delivered from a system across a range of voltages. This indicates the maximum operating conditions a device could run at. The process involves sweeping the potential applied to a system from a low to high voltage at a specific scan rate and recording the resulting current. The exact shape of the plotted graph depends on things like the rate of electron transfer steps or scan rate, however an example of a typical LSV curve is shown in Figure 20 and some key aspects are highlighted[118,119].

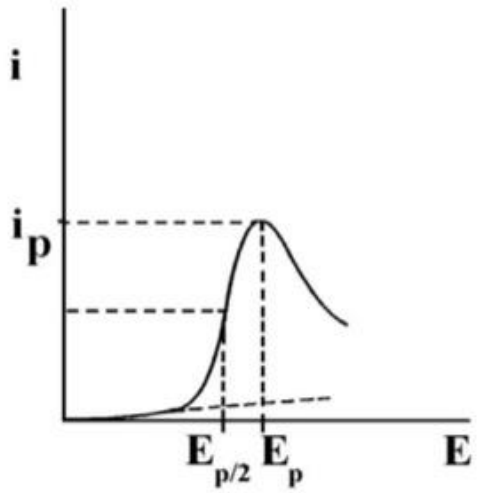


**Figure 20** – *An example of an LSV curve, with potential on the x-axis and current on the y-axis. $I_p$ and $E_p$ represent peak current and potential, respectively, and $E_{p/2}$ represents half-peak potential*[119].

$I_p$ provides information on things like the number of electrons involved in the reaction and the presence of coupled chemical reactions, whereas $E_p$ provides data on the reactants themselves. The measured values conform to the Nernst equation, which is shown in Equation 3:

(3) $$E = E° + \frac{RT}{nF} \ln \frac{[O]_t}{[R]_t}$$

Where E is the applied potential, E° is the standard electrode potential, R is the gas constant, T is the temperature, n is the number of electrons, F is Faraday's constant, $[O]_t$ is the concentration of oxidised species at time, t, and $[R]_t$ is the concentration of reduced species at time, t[120].

At equilibrium, the ratio of oxidised and reduced species is equal. When an LSV test starts, the system is polarised by a low potential meaning reduction will occur – this increases the number of reduced species present thus giving rise to a negative current. As time increases and the voltage is swept to higher values, the concentration of oxidised species increases thus increasing the number of released electrons, which results in a positive current being measured.

The characteristic trait of an LSV curve is that the current measured will plateau at a certain voltage, and then drop. This is caused by diffusion layer thickness on the electrode surface rising until the flux of reactants is not sufficient to meet the conditions of the Nernst equation, and so the current starts to drop due to a reduced concentration of oxidised species[121]. This explains why scan rate affects the shape of an LSV curve. If the scan rate is low, the diffusion layer thickness will increase thus reducing the magnitude of the concentration gradient, which in turn reduces flux and so reported maximum current density. Scan rate should be appropriately optimised when measuring PEMWE device performance.

### 2.1.2. Chronopotentiometry

In chronopotentiometry, a fixed current is delivered between the working and counter electrodes and any changes in potential are measured as a function of time. Chronoamperometry works on the same basis, however the applied potential is constant and the variation in current is recorded over time. By constantly inducing flux within the system, fresh reactants are regularly delivered to the electrode surface and so any changes in performance can be said to be caused by the degradation of system components. These include but are not limited to catalyst dissolution and membrane degradation.

Chronopotentiometry is the primary means of determining the stability of novel cell components for PEMWE. However, a real working electrolyser is expected to run for around

40,000 hours and running chronopotentiometry tests for this long is not feasible in practice. Additionally, these experiments operate at a fixed current density, and performing stability tests under static operating conditions is unsuitable as previously discussed. Future chronopotentiometry experiments could be modified to include cycling of operating conditions, to better emulate the true operating conditions of a working electrolyser, thus providing more accurate stability data.

### 2.1.3. Electrical Impedance Spectroscopy

EIS is an extremely powerful technique that has been harnessed across a range of research fields from biosensing to electrocatalysis to provide in depth data regarding an electrochemical system. A small sinusoidal alternating current (potentiostatic) or voltage (galvanostatic) at frequencies between 1 mHz - 1 MHz is applied to a system at equilibrium and the response is measured[122]. Due to the small scale that EIS works on, it can recognise nearly any artefact altering the conductivity of a system, making it useful for investigating changes within an electrochemical cell – from the electronic double layer to surface roughness.

Impedance simply refers to the opposing force a current faces in an electric circuit and is measured in Ohms. It differs from resistance as it comes from an alternating source and so does not follow Ohm's law[123]. This parameter is measured by fitting recorded values to an electrical equivalent circuit, which in this instance is a Randel's cell[124]. Impedance, Z, is a product of solution resistance, $R_u$, electronic double layer charge, Q, charge transfer resistance, $R_{ct}$ and the Warburg Element, $Z_w$. However, the Warburg element accounts for diffusion of ions and the HER/OER is known to be under complete kinetic control in acidic conditions and so this can be removed for simplicity[125]. This gives rise to the model circuit shown in Figure 21.

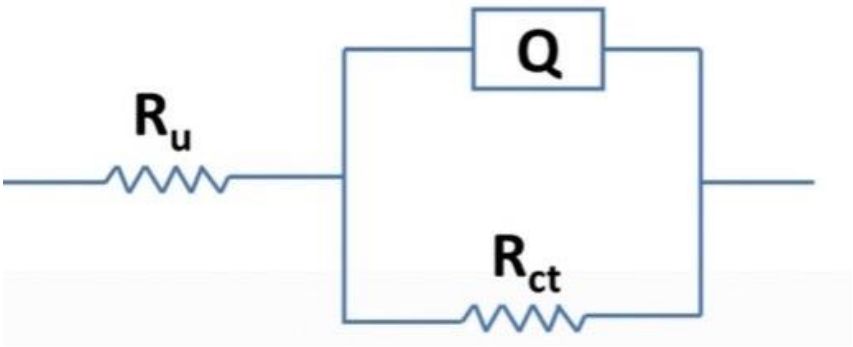


**Figure 21** - *Electronic equivalent circuit of a simple Randel's cell, modified for water electrolysis in acidic conditions*[125].

These components can then be inserted into the following equations to determine real (Equation 4) and imaginary components (Equation 5) of the impedances[126]:

(4) $$Z' = R_u + \frac{R_{ct}}{1+R_{ct}^2Q^2}$$

(5) $$Z'' = \frac{R_{ct}^2Q}{1+R_{ct}^2Q^2}$$

The equations are then manipulated across the range of frequencies selected and compiled by online software, which produces a Nyquist plot allowing for a visual representation of the results. The small scale EIS works on often leads to challenges in results interpretation, however the technique is invaluable in electrochemical research due to its ability to rapidly assess parameters such as overall system resistance.

## 2.2. Analytical and Characterisation Techniques

Analytical and characterisation techniques are crucial when aiming to understand different phenomena observed in a system. The techniques used in this study will be subsequently discussed.

### 2.2.1. Gas Chromatography

Gas chromatography is routinely employed by researchers aiming to determine the molecular make-up of a complex sample through a means of separation. The machine operates within a

large oven and has two phases – a solid or liquid stationary phase, and a gas mobile phase that carries the sample through the stationary phase unidirectionally[127]. Samples can be injected into the system via syringe as either a liquid or gas, however they must be vaporised at temperatures below 300 °C. Additionally, the compounds seeking to be identified must not decompose or react with either phase, as this would provide spurious results[128].

Once the sample is injected into the GC, it is moved across the stationary phase by the mobile phase - commonly argon gas. The stationary phase can either be in the form of a packed column (a large solid column filled with small particles of high molecular weight polymer) or a capillary column (a thin silica tube with the stationary phase bonded to the surface)[129]. Different compounds within the sample traverse through the column at different speeds, and so they elute at different rates. This gives rise to unique retention times which a detector and computer use to produce a chromatogram, thus allowing the identification of known compounds and their concentrations within the sample. This process is summarised in Figure 22.

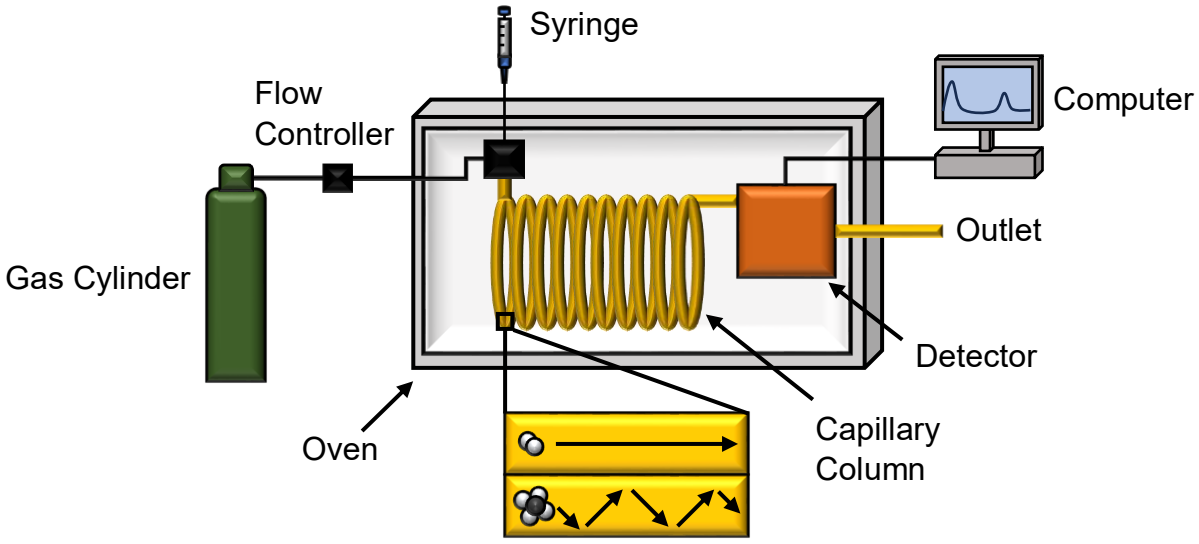


**Figure 22** – *Schematic of a working gas chromatography machine. A syringe injects the sample into the machine, where it is met by a controlled flow of argon. The sample is then moved through the capillary column. Smaller molecules interact with the walls less so pass quickly, and larger molecules interact more so are held within the column for longer. Different gases then elute at different rates, where they are detected and then released from the system.*

The retention time of each compound is the key parameter measured in gas chromatography analysis and is based upon the interaction of the anolyte with the stationary phase[130]. Larger compounds will have an increased number of intermolecular interactions - like hydrogen

bonding or dipole-dipole interactions - with the stationary phase surface, meaning that they will take longer to elute from the column. Smaller molecules will interact less and so will be moved along at faster rates. Other factors such as column temperature, flow rate and column degradation can also influence retention time[131]. These times are relative and vary across each machine, and as such are only used for the identification of compounds. When calculating compound concentrations, it is the area under the peak in the chromatogram that is of significance[129].

When researching PEMWE, gas chromatography is commonly used to measure the head space of a system to evaluate product gas composition. The use of on-line gas chromatography machines has been reported in the literature, and this describes the use of a machine which is directly linked to the headspace of a sample using a thin tube[132]. This allows for more accurate results as human error from sampling is eliminated and for measurements to be taken at increased intervals thus providing information on how products evolve over time.

### 2.2.2. Scanning Electron Microscopy

Scanning electron microscopy is an ex situ characterisation technique which allows for the imaging of samples above the diffraction limit of traditional light based microscopes. This means that advanced scanning electron microscopes can image samples at > 1,000,000 times magnification with single nanometre resolution, whereas conventional optical microscopes can only image at around 1000 times magnification[133]. The technique uses a charged electron gun to systematically scan a sample, giving rise to surface-electron interactions that are subsequently detected and processed computationally to form an image. Figure 23 summarises this process[134].

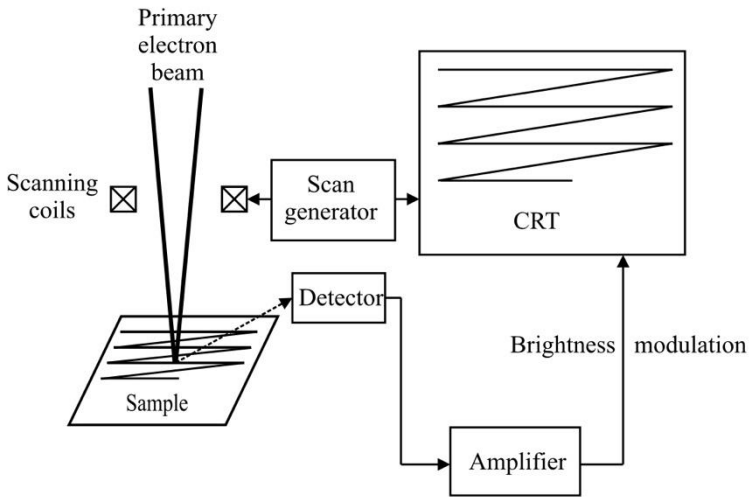


**Figure 23** - *Schematic showing a simplified explanation of how a SEM image is produced*[134].

The electron gun is formed by delivering a high current under vacuum to tungsten or lanthanum hexaboride filaments, causing heating to temperatures so high electrons are emitted from the surface. These high energy electrons (2-40 keV) are focused through a series of lenses to produce a monochromatic beam that hits the sample. This interaction produces secondary and backscattered electrons which are collated to produce the image. X-rays and auger electrons are also produced, however they do not form part of the SEM image[135].

Secondary electrons are the strongest signal measured and are caused when weakly bound electrons get released from the sample. They are relatively low in energy and so are only released from first few nanometres of the surface, meaning they are responsible for surface structure imaging. Backscattered electrons are the product of incident electrons penetrating deep into an atom, causing wide angle scattering. These electrons are high in energy and so come from deep within the surface. Heavier atoms cause more backscattering, meaning this signal can be used to identify bright spots in the image caused by high atomic number elements[136].

SEM is routinely used in water electrolysis research as it allows for simple characterisation of surfaces. This type of microscopy is particularly useful when analysing electrodes – from measuring GDL porosity to catalyst surfaces before and after device operation. However, the

high energy electron beam can destroy samples rapidly and as the gun operates under vacuum, the imaging of hydrated surfaces is not possible.

### 2.2.3. Inductively Coupled Plasma-Optical Emission Spectroscopy

Inductively coupled plasma-optical emission spectroscopy is one of the most advanced techniques for measuring trace elements within a sample. It works in a similar way to classic optical emission spectroscopy, however uses plasma to break down the sample into its elemental and ionic components. It can detect several elements at once by using an increased number of photon detectors, even at concentrations below the ng per ml level[137]. Due to the weak signal measured at such low concentrations, a high resolution optical spectrometer is used to refine the signal. Figure 24 shows the apparatus required to conduct an ICP-OES experiment[138].

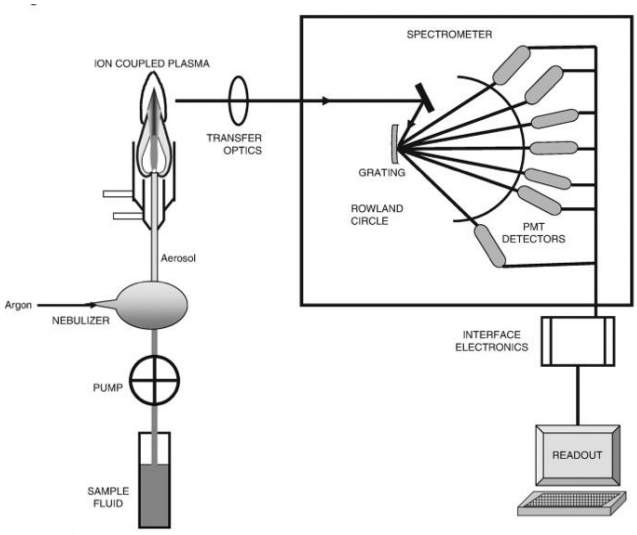


**Figure 24** - *Schematic representing an inductively coupled plasma-optical emission spectrometer*[138].

Plasma is a state of matter characterised by the partial or full ionisation of a substance, which provides unique properties useful for research application[139]. To produce the plasma, a high-power radio frequency is applied to a copper coil which generates a strong magnetic field. Argon is then flowed through the coil causing partial ionisation. This generates free electrons which go on to further ionise the sample through a cascade effect, thus making the plasma[140].

Next, the sample is nebulised, and droplet size is carefully regulated before the sample is mixed with argon gas and sprayed as an aerosol through the plasma. The extreme temperatures cause the subsequent desolvation, vaporisation, atomisation, and ionisation of the sample, leaving only pure atoms and ions[138]. Electrons within these atoms and ions are then excited to a higher state temporarily, and upon return to the ground state release photons through a process known as atomic emission (Figure 25).

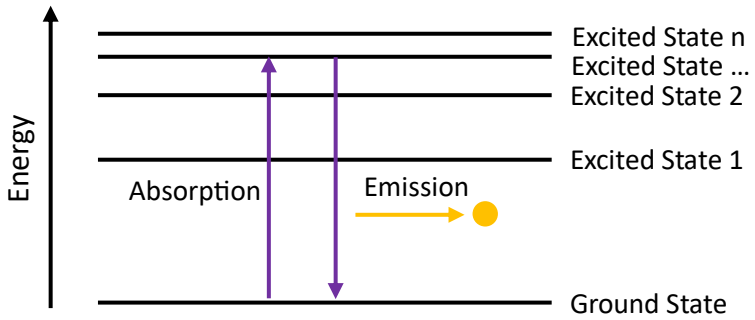


**Figure 25** - *Diagram showing how atomic emission occurs. An atom exists in the low energy ground state before absorbing energy to place it in a high energy excited state. The atom exists here temporarily before falling back to the ground state, and in doing so releasing energy in the form of a photon - shown by the yellow circle. This process is known as emission.*

As each element contains discrete energy levels (represented in Figure 25 as excited states), the allowed transitions within an element will correspond to a specific wavelength of light. This wavelength will be different across all elements and possible transitions (i.e different between excited state 1 → ground state and excited state 2 → ground state)[141]. This allows multiple detectors to measure the wavelengths of incoming photons and compare them against known standards, to correctly identify elemental composition and concentration of a sample.

The technique is particularly useful in electrocatalysis research when aiming to quantify the leeching of the electrocatalyst into solution. This was reported by Faqeeh and Symes in 2023[142].

# 3. Experimental Methods

## 3.1. System Components

The flow cell used within this study followed the same basic design principles described in Section 1.3. The aluminium end plates used were 106 × 106 × 10 mm in size. Each plate had 8 large holes evenly distributed around the perimeter. A central square was marked by 4 small holes which framed 2 larger holes. The PTFE insulator plates were nearly identical in structure; however, the two central holes were threaded to allow the attachment of polypropylene hose barbs. The cell was held together by 8 M8 hex bolts (8 × 75 mm, fully threaded) which were placed through outer holes of the end and insulator plates. Each bolt was tightened to a compression force of 5.65 N m. Two titanium plates (grade 2, 3 mm thickness) were used as current collectors and each had six serpentine flow channels (1 mm wide, 1 mm deep) engraved on the surface to deliver reactants and remove evolved gases. PTFE gaskets (0.13, 0.25, and 0.51 mm thick) (FuelCellStore) were placed on either side of each current collector to prevent leakage.

The cathode was a 37 mm square of platinum on carbon cloth with a loading mass of 0.5 $mg_{Pt}$ $cm^{-2}$ (0.4 mm thick, FuelCellStore). The anode was produced in-house and consisted of a 37 mm square titanium fibre felt GDL (0.2 - 0.3 mm thick, FuelCellStore), a titanium microparticle MPL and an $IrO_2$ catalyst layer at a loading mass of 1.5 mg $cm^{-2}$. The active area of the flow cell was 13.7 $cm^2$. The membranes used were Aquivion® E95-1S, Nafion™ 117 and PFSA D170-U (FuelCellStore). Herein, these membranes will be referred to as Aquivion®, Nafion™ and D170-U.

A Fisherbrand GP1100 General Purpose peristaltic pump was used to flow deionized water (15 MΩ resistivity) at a rate of 40 ml $min^{-1}$ through Norprene tubing (4.78 mm diameter, Merck Life Science UK Limited) attached to hose barbs in and out of the cell. The anolyte and catholyte were held in 2 litre media bottles, each with 4 screw caps on the lid. Hot plates were used to heat the system to 60 °C, which was monitored by K-type thermocouples at the inlet/outlet of the cell. The data was sent to a PicoLog TC08 data logger and PicoLog Software.

A biologic SP-150 potentiostat and an 80 A booster were used to power the system. The apparatus is summarised in Figure 26.

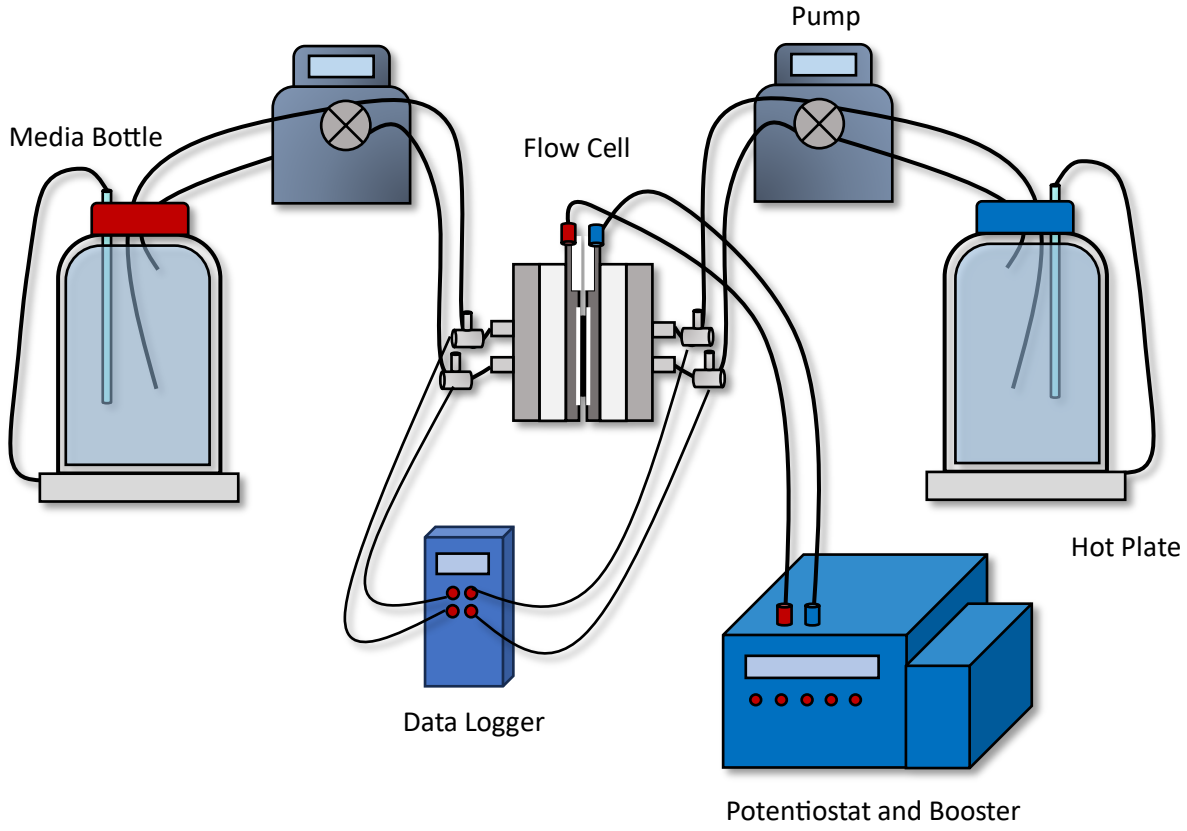


**Figure 26 –** *Simplified schematic showing the apparatus used for electrochemical testing in this study.*

### 3.1.1. General Preparation

The membranes were cut into 106 mm squares on a clean surface using a scalpel and submerged in deionised water for at least 24 hours prior to use. Each membrane was shipped in the acid form, meaning no pre-treatment was required.

The gaskets were prepared via the following steps. A 0.51 mm thick PTFE sheet was cut into two 66 mm squares using a guillotine. Each of these squares was aligned with the central squares on the insulating plates and two holes (slightly larger in size than the hose barbs in corresponding positions) were removed. Next, two more 66 mm PTFE squares were cut, however each square came from a sheet 0.25 and 0.13 mm in thickness, respectively. A central square was cut and removed from each of these sheets at an indent of approximately 10 mm.

### 3.1.2. Anode Preparation and Production

The number of commercially available and suitable PEMWE anodes is somewhat limited due to the many different possible configurations. There are spinout companies capable of producing customisable titanium electrodes with iridium coatings, however it was decided that producing the anode in-house was the optimal route to follow. The anode was produced via the CCS method by the air-spray deposition of a MPL suspension and catalyst ink on to a titanium fibre felt GDL. This method was favoured over the CCM due to simplicity.

To produce the MPL, a glove box operating under a nitrogen atmosphere was used to weigh 2.5 g of 5 μm titanium microparticles (US Nanomaterials Research) into a vial. The vial was sealed using a septum and removed from the glovebox. A syringe was then used to add 2.5 mg of 5 % Nafion™ solution (Ion Power Inc) and 10.0 g of isopropanol to the vial. The septum was then removed and replaced with a cap. The vial was placed in an ultrasonic ice bath for 15 minutes, before being removed and having 10.0 g of ethylene glycol added. The solution was then sealed again and placed back in the ultrasonic ice bath for 1 hour. After this, the vial was kept in a refrigerator at 4 °C until required.

The CL was prepared from an ink composed of 65 % $IrO_2$ (99.9%) (Sigma Aldrich), 20 % Carbon black (Carbon black, acetylene, 50 % compressed, 99.9+%) (ThermoScientific) and 15 % Nafion™ solution (5%) (Ion Power Inc). To successfully reach the desired loading mass a total mass of 362.6 mg was required, so reactants were scaled to meet this requirement. Additionally, 5.1 ml of isopropanol was added to create the ink.

The aforementioned compounds were added to a glass airbrush jar and a glass stirring rod was used to breakdown any large clumps. A small amount of isopropanol was used to wash any catalyst ink off the stirring rod and back into the vial. The solution was then sealed and placed in an ultrasonic ice bath for 1 hour, with checks performed every 20 minutes to monitor temperature. It should be noted that the water level of the ultrasonic bath should cover up to the shoulder of the jar and no more. After the allotted time, the solution was stirred with the glass rod for five minutes, sealed and placed back into the ultrasonic ice bath for another hour. Following production, the catalyst ink was kept in the refrigerator at 4 °C until required. The ink was always be made for same day use, as if left for longer the homogeneity of the ink is reduced.

The anode was produced via the following steps. The foamboard used as a support was 5 mm thick (Amazon). The airbrush used was a Royal Airbrush AB-182 and the air compressor was a Royal Max TC-80T – Single Piston Compressor with a tank size of 3 litres.

1. The oven was set to 200 °C.
2. A 37 × 37 mm square of titanium fibre felt was cut using a guillotine and the mass recorded.
3. A 100 × 100 mm square of foam board was then cut using a scalpel. The titanium substrate was placed in the middle of the foam board and a scalpel was used to trace the outline, at around half the depth of the foam board. The metal square was placed aside, and a smaller square was removed from the centre of the foam board - around 20 mm in length. The remaining part of the larger half-depth square was then removed by inserting the scalpel parallel with the foamboard and cutting. This creates a support with an appropriately sized edge to hold the titanium substrate in place during air-spraying. An example of how the support looked is shown in Figure 27.

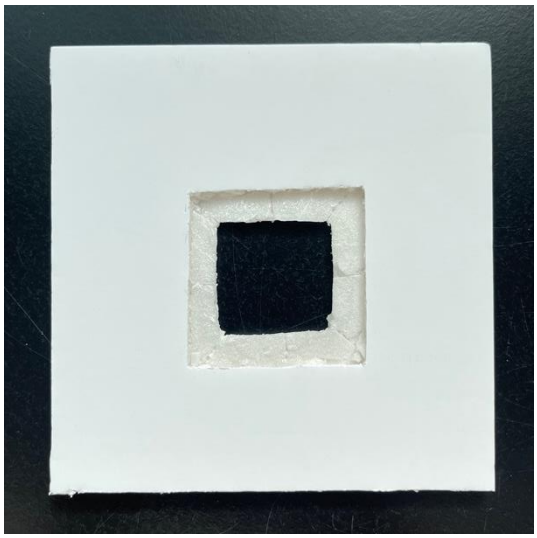

**Figure 27** – *Image showing how the foam board support should look after preparation.*

4. Next, the MPL suspension was removed from the fridge and shook vigorously to perturb any settled microparticles at the bottom of the vial. A glass dropper was used to add approximately 1 ml of the suspension to a glass airbrush jar with an airbrush connector lid.

5. The airbrush was then checked for cleanliness and the knob at the back of the airbrush was fully rotated 2.5 times in the anticlockwise direction to control the output. The airbrush was connected to the jar and air compressor, which was set to 1 bar.
6. In a fume hood, the foamboard holding the substrate was placed against the back wall. From a distance of 10 cm, the airbrush was held perpendicular to the foamboard and the substrate coated with a thin layer of MPL. The airbrush was moved in a clockwise direction around the square, starting from the top left hand corner. Once the rotation was complete the airbrush was directed to the centre of the substrate for a few seconds to ensure the surface was evenly coated.
7. The substrate was then removed from the support and placed in the oven for 7 minutes.
8. The dry mass of the substrate was recorded and spraying repeated until 10 – 15 mg of MPL was deposited. When the substrate was placed back on the support, care was taken to insert it at the same position as before, and the foamboard was rotated by 90 ° to ensure an even distribution of MPL.
9. The oven temperature was reduced to 100 °C and the recently prepared catalyst ink was placed in a freezer at − 20 °C for 15 minutes.
10. A new airbrush was prepared using the same conditions described in step 5.
11. The same procedure for spraying described in step 6 was then repeated, however the MPL suspension was replaced with the full jar of catalyst ink. To reach the desired loading mass 31.6 mg of ink needed to be deposited on the substrate surface, meaning many coats were required. Due to this, the substrate was sprayed four times before being placed in the oven to dry for 5 minutes and the catalyst ink was placed back in the freezer.
12. The substrate was then weighed, and the mass recorded. A cycle of four sprays added approximately 10 mg in total, so this process was repeated twice to add a total of 20 mg to the substrate.
13. After this, care was taken to only spray the substrate once between weighing, as it was crucial to not overshoot the catalyst mass. The spray, dry and weigh process was repeated until the desired mass was reached.
14. The substrate was then placed in th oven for 1 hour at 100 °C to anneal the catalyst layer before being removed.

After production, the anode was incorporated into the flow cell as soon as possible to minimise any changes in surface structure.

### 3.1.3. System Assembly

The threaded end of a hose barb was wrapped in 15 cm of PTFE tape and a wrench was used to insert the hose barb into a central hole in the insulating plate, ensuring it was flush with the opposing side. This process was repeated for the 3 remaining hose barbs, which provided the inlet/outlet connections for the flow cell.

Next, a large cork ring was placed on the bench and the components were assembled flat in the order shown in Figure 28, from left to right.

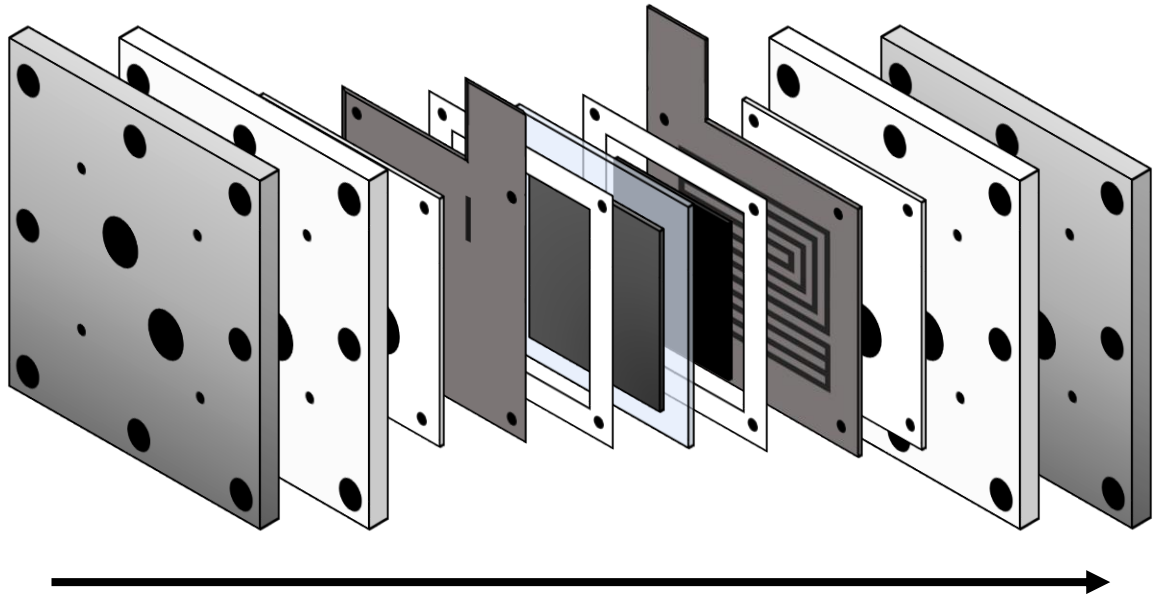

**Figure 28 –** *Schematic showing an exploded diagram of the flow cell. From left to right: end plate, insulating plate, gasket (0.51 mm thick), current collector, gasket (0.13 mm thick), anode, PEM, cathode, gasket (0.25 mm thick), current collector, gasket (0.51 mm thick), insulating plate and end plate.*

Please note: After the first end plate was placed down, 4 thin metal rods were inserted into each of the holes forming the central square. All other components were aligned using these rods to ensure minimal movement during assembly.

A bolt was then placed through each of the outer holes of the cell, which was kept flat while a washer and nut were attached from below. These were tightened as much as possible by hand before the cell was lifted vertically. A torque wrench was set to 5.65 N m and used to tighten each bolt. When sufficient compression was reached, the wrench would click and resist.

Following this, one short and one long piece of tubing were wrapped in PTFE tape at one end. The wrapped ends were inserted into opposite sides of a T-type tube connector and a thermocouple was placed in the perpendicular end. The short piece of tubing was fixed to a hose barb while the longer piece was run into the media bottle. This process was repeated for the other 3 hose barbs and the tubing was run like a waterfall, so the inlet was positioned above the outlet. The tubing was inserted through the caps in the media bottles and a silicon seal was used to restrict movement. The inlets were made to be long enough so that they reached well below the predicted minimum water level of the media bottle. The outlets only ran to the neck of each bottle. The bottles were placed on a hot plate and a thermometer was run through one of the caps and a silicon seal. A final cap was used to close the fourth hole in the media bottle.

Lastly, the cables from the potentiostat were fixed to the current collectors via claw clips.

### 3.2. Electrochemical Methods

All electrochemical testing was conducted at 60 °C and data was acquired using EC-Lab software version 11.43. The LSV measurements were performed between 0 and 2 V at a scan rate of 10 mV $s^{-1}$. The chronopotentiometry measurements were performed at a current density of 1 A $cm^{-2}$ for 100 hours. Due to electroosmotic drag - which draws water from the anode side to the cathode side – after approximately 48 hours a third pump was used draw water from the cathode back to the anode. The EIS tests were performed from 0.5 Hz to 20 kHz. Data was analysed using Nyquist plots. All graphs presented were produced using Origin Lab Version 10.00154.

### 3.3. Analytical and Characterisation Methods

The gas chromatographer used was an Agilent 8860, which used Agilent OpenLab CDS Acquisition software version 2.6. Hydrogen crossover at the anode was measured by purging the reservoir with argon gas for 30 minutes at 1 bar, and then running the system for 1 hour at a current density of 1 A $cm^{-2}$. The anolyte headspace was then tested using gas chromatography for the presence of hydrogen. Electrochemical testing was then performed and gas chromatography was repeated to measure for any changes in hydrogen crossover at the anode.

A Tescan Clara ultra-high resolution SEM with a field emission electron gun operating at 5 keV was used to image the membrane surface. A Polaron SC7460 high resolution sputter coater

was used to coat the samples in a thin coating of gold-palladium nanoparticles to enhance image resolution. Data was processed and analysed using Tescan Essence software version 1.2.2.0.

ICP-OES data was gathered using an Agilent 5900 and an Agilent SPS4 autosampler. Samples were tested for iridium and platinum content and diluted five-fold using deionised water prior to analysis. The machine has a lower detection limit of a few parts per billion.

# 4. Results and Discussion

## 4.1 Performance, Stability and Hydrogen Crossover

The following section presents data gathered from the electrochemical testing and characterisation of each membrane. The results are summarised in Table 3.

| Membrane | Current Density at 2 V (A $cm^{-2}$) +/− SD | Degradation Rate (mV $h^{-1}$) +/− SD | Hydrogen Crossover at Anode (mol $l^{-1}$) +/− SD | | Pinholes Observed After Use (Yes/No) | $IrO_2$ Concentration of Anolyte After Stability Test (mg $l^{-1}$) +/− SD |
|---|---|---|---|---|---|---|
| | | | Before | After | | |
| **Aquivion®** | 1.01+/− 0.06 | 0.62 +/− 0.20 | 0.12 +/− 0.01 | 0.27 +/− 0.03 | No | 0.06 +/− 0.01 |
| **Nafion™** | 0.96 +/− 0.02 | 0.97 +/− 0.34 | 0.15 +/− 0.02 | 0.33 +/− 0.06 | Yes | 0.04 +/− 0.02 |
| **D170-U** | 1.10 +/− 0.09 | 0.92 +/− 0.10 | 0.12 +/− 0.05 | 0.41 +/− 0.08 | Yes | 0.07 +/− 0.06 |

**Table 3 –***A summary of the results gathered in this study. In all columns with a numerical value, the data given is an average of 3 tests, +/− the first standard deviation (SD). The first column states the membrane tested, the second shows the current density reported at 2 V (A $cm^{-2}$), and the third shows the degradation rate (mV $h^{-1}$). In the fourth column, the hydrogen crossover at the anode after 1 hour of operation before/after the chronopotentiometry test is shown (mol $l^{-1}$). Finally, the presence of pinholes on the membrane surface after use is stated, followed by the $IrO_2$ concentration at the anode after the chronopotentiometry test (mg $l^{-1}$).*

Table 3 shows that Aquivion® gave similar results to Nafion™ across all parameters. It also shows the only parameter Aquivion® and D170-U performed significantly different in was hydrogen crossover at the anode after chronopotentiometry. The hypothesis between Nafion™ and D170-U was supported when investigating performance, however the membranes were similar in all other areas tested. The standard deviations presented in Table 3 show that the results of each membrane overlap with others in many cases - indicating that the effects of side chain length on device operation is not significant and that D170-U performs at a similar standard to the other two membranes.

### 4.1.1 Performance

To assess the performance of each membrane, LSV was used to determine system current density across a range of voltages. The performance of each membrane is shown in Figure 29.

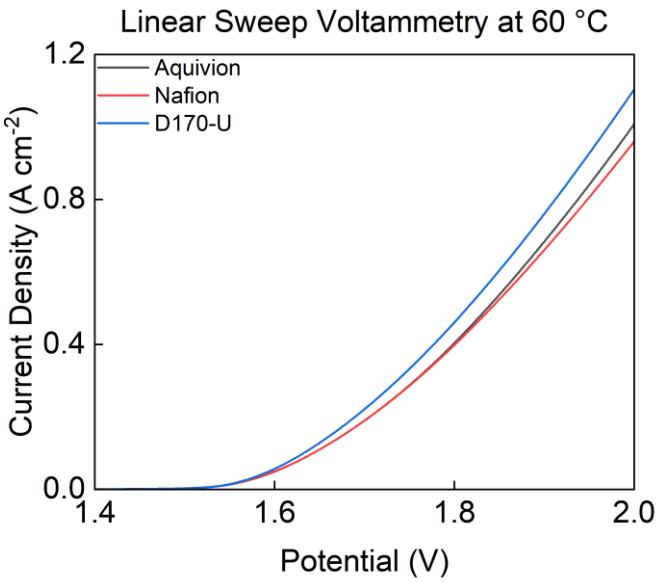


**Figure 29** – *LSV plot showing the current density (A cm$^{-2}$) of Aquivion®, Nafion™ and D170-U across a voltage range of 1.4 – 2.0 V at 60 ℃. The grey line represents Aquivion®, the red line represents Nafion™ and the blue line represents D170-U.*

The figure above shows that at 2.0 V, D170-U delivered the highest current density - operating at 1.10 A cm$^{-2}$. This was followed by Aquivion® and subsequently Nafion™, operating at 1.01 and 0.96 A cm$^{-2}$, respectively.

When the standard deviations shown in Table 3 are accounted for, the performance of Aquivion® is comparable to both long side chain membranes tested. This does not support the hypothesis, which proposed Aquivion® would display superior performance. The hypothesis was stated for several reasons - firstly, Aquivion® was the thinnest membrane tested, and so should have the lowest ohmic resistance and consequentially the highest performance[37,143]. EIS supported this statement, as the resistivity of the system containing Aquivion® was 0.017 Ohms, compared to that containing Nafion™ and D170-U, which gave values of 0.021 and 0.019 Ohms, respectively. Additionally, a higher proton conductivity positively impacts device performance and it was found that Aquivion® (0.16 S cm$^{-1}$) reported a higher value than both Nafion™ (0.08 S cm$^{-1}$) and D170-U (> 0.10 S cm$^{-1}$)[144,145]. This information supports the

hypothesis that Aquivion® will display superior performance, however the results suggest that the performance of Aquivion® is not significantly different to the other two membranes.

When comparing D170-U against Nafion™, the data presented shows that D170-U yielded optimum performance. However, these results are only different by the first standard deviation, meaning there is only a 68 % chance the results are significantly different.

As Nafion™ is the most popular membrane used in PEMWE, there is much data regarding its performance in the literature. Across 11 publications, it was reported that Nafion™ 117 required between 1.65 – 1.95 V to reach 1 A $cm^{-2}$ [106]. These are not dissimilar to the values reported in this study, and the slightly reduced performance may be accounted for by reduced iridium loading mass and temperature. For Aquivion®, there are fewer reports in the literature. One paper reported an Aquivion® membrane reaching a current density of 1.9 A $cm^{-2}$ at 1.8 V [59]. The higher performance reported in this paper is likely due to the use of an increased iridium loading and a thinner membrane. There were no reported studies on D170-U. Increasing the loading mass of iridium would have made this study more comparable to the literature.

### 4.1.2. Stability

Chronopotentiometry was used to measure the degradation rate of each membrane (Figure 30).

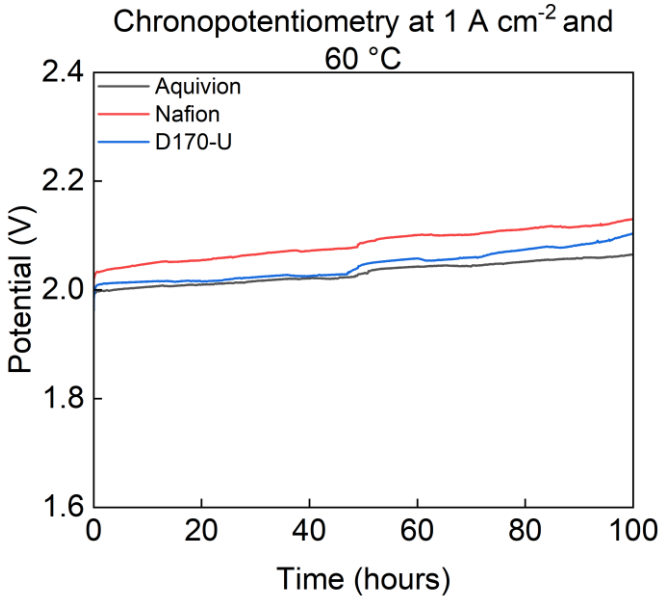


**Figure 30** – *Chronopotentiometry graph showing the operating potential (V) of Aquivion®, Nafion™ and D170-U over 100 hours at 1 A $cm^{-2}$ and 60 °C. The grey line represents Aquivion®, the red line represents Nafion™ and the blue line represents D170-U.*

The initial operating potential of each membrane is consistent with the literature and EIS data, in that thicker membranes give greater ohmic resistance to the system, thus resulting in a higher potential required to reach a fixed current density[37]. Degradation rates calculated between hours 1-100 reveal Aquivion® had the lowest degradation rate (0.62 mV $h^{-1}$), followed by D170-U (0.94 mV $h^{-1}$) and finally Nafion™ (0.97 mV $h^{-1}$).

Given the data in Table 3, when considering short side chain vs long side chain the results do not support the hypothesis. This is because all membranes showed similar degradation rates within one standard deviation, and so the results cannot be said to be significantly different. This could be explained by the increased thickness of Nafion™ and D170-U, which would reduce the degradation rate[146]. Membranes of identical thickness would have provided a fairer comparison, however this was not possible due to a lack of availability.

It was also hypothesised that Nafion™ would demonstrate a lower degradation rate than D170-U, however this was not observed. Nevertheless, the rates reported are very similar and the rather large standard deviation of Nafion™ in Table 3 indicates some unreliability in the data.

In an industrial setting, degradation rates of 1 $\mu$v $h^{-1}$ are deemed acceptable[27]. Despite this, there are many papers within the literature reporting values in the mV $h^{-1}$ region. One paper reported the use of an Aquivion® membrane that degraded by approximately 0.30 mV $h^{-1}$ over the first 100 hours, and then by 15 $\mu$v $h^{-1}$ for the remaining 1000 hours of the stability test[147]. The authors stated this was due to MEA conditioning, which may also be present in this study however an extended durability test would be required to identify this. In another study, a thinner version of Aquivion® degraded at a rate of 1 mV $h^{-1}$ over 100 hours at 1 A $cm^{-2}$ [59]. This pairs well with the degradation rate of Aquivion® measured in this study, as it supports the literature stating that thicker membranes show lower degradation rates[146].

It would have been beneficial to run each test for several hundred hours, as in practice membranes are required to run for much longer than 100 hours. Despite degrading at similar rates to Aquivion® and Nafion™ in the chronopotentiometry test, whether or not D170-U could compete in an industrial setting cannot be said.

It could have also been useful to run an accelerated stress test in order to identify the strongest/weakest membrane. This involves rapid cycling of conditions known to cause the most degradation (such as fluctuations in operating voltage/current), thus inducing degradation mechanisms at faster timescales than would be observed in practice[148].This would allow the determination as to whether or not D170-U could compete with the other membranes in an industrial setting.

### 4.1.3. Hydrogen Crossover

Hydrogen gas crossover at the anode is known to be a cause/effect of system degradation. This was investigated via gas chromatography of the anolyte headspace after 1 hour of bulk electrolysis, before and after the chronopotentiometry test. The results are shown in Figure 31.

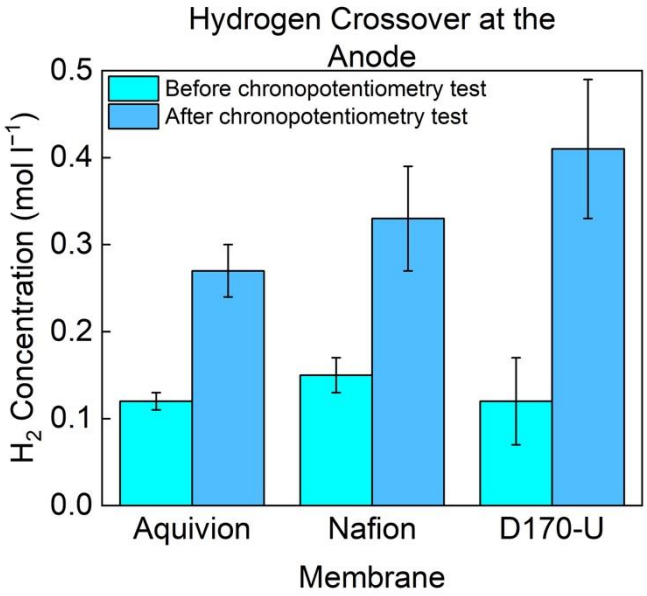


**Figure 31** – *Bar chart showing the concentration of hydrogen gas at the anode (mol $l^{-1}$) for each membrane after 1 hour of bulk electrolysis at 1 A $cm^{-2}$, before (light blue) and after (dark blue) the chronopotentiometry test. Error bars representing the first standard deviation are included at the top of all bars in black.*

Figure 31 shows that before the stability test, all membranes had a similar volume of hydrogen permeating from the cathode to the anode (Aquivion® = 0.12, Nafion™ = 0.15 and D170-U = 0.12 mol $l^{-1}$). After the chronopotentiometry test, all of the membranes demonstrated increased hydrogen crossover. This was observed the least in Aquivion®, which rose to 0.27 mol $l^{-1}$, followed by Nafion™ and then D170-U which increased to 0.33 and 0.41 mol $l^{-1}$, respectively.

The results show that after the chronopotentiometry test, Aquivion® and Nafion™ demonstrated comparable hydrogen crossover at the anode. While the results of Aquivion® and D170-U do not directly overlap, both overlap with Nafion™, suggesting no membrane performed significantly different than the others. The comparable results may have been due to the increased thickness of Nafion™ and D170-U which would reduce gas crossover.

To better understand these results, ex-situ characterisation was performed.

## 4.2. Ex-Situ Characterisation

The results presented suggest that during device operation, the system is undergoing some form of degradation. It is known that the two weakest components of a PEM electrolyser are the membrane and the OER catalyst, and so these were investigated for degradation.

### 4.2.1. OER Catalyst Degradation

The issue surrounding OER catalysts is not owed to the activity/stability of iridium - but with the extremely high cost which requires loading masses to be kept at a minimum. At these low loading masses, common catalyst degradation mechanisms – such as dissolution, agglomeration, or oxidation – impact performance at a greater level, meaning they are often responsible for device failure[37]. Catalysts have also been reported to migrate through the membrane to the opposing side, where they disrupt the desired reaction and reduce the efficiency of the cell[149].

To determine if the iridium catalyst used displayed a significant level of degradation, ICP-OES was performed on the anolyte and catholyte to check for catalyst leaching after the chronopotentiometry test (Table 4).

| Membrane | Anolyte | | Catholyte | |
|---|---|---|---|---|
| | $IrO_2$ Concentration (mg $l^{-1}$) | Pt Concentration (mg $l^{-1}$) | $IrO_2$ Concentration (mg $l^{-1}$) | Pt Concentration (mg $l^{-1}$) |
| Aquivion® | 0.058 +/− 0.01 | < MDL | < MDL | < MDL |
| Nafion™ | 0.040 +/− 0.02 | < MDL | < MDL | < MDL |
| D170-U | 0.068 +/− 0.06 | < MDL | < MDL | < MDL |

**Table 4 –** *Table showing the results from the ICP-OES test of the anolyte and catholyte from each membrane after the chronopotentiometry test. MDL stands for minimum detection limit.*

The results show in all cases there was no detectable catalyst migration through the membrane. Additionally, no platinum was detected in any of the samples – indicating excellent stability of the cathode catalyst. Moreover, very high stability and attachment of the anode catalyst is shown, as each anolyte reported an iridium concentration ≤ 0.1 mg $l^{-1}$.

At present, there was little to no information in the literature regarding iridium concentration in the anolyte and catholyte of PEMWE devices. However, iridium is stable for many hundreds of hours under PEMWE conditions and the results demonstrated minimal detachment of the anode catalyst (Table 4)[36]. This suggests that OER catalyst failure was not the cause of degradation observed in this study.

### 4.2.2. Membrane Degradation

The other primary cause of degradation in PEM electrolysers is membrane damage. To determine if this was present in the study, each membrane was imaged before and after the described electrochemical testing was performed. This is shown in Figure 32.

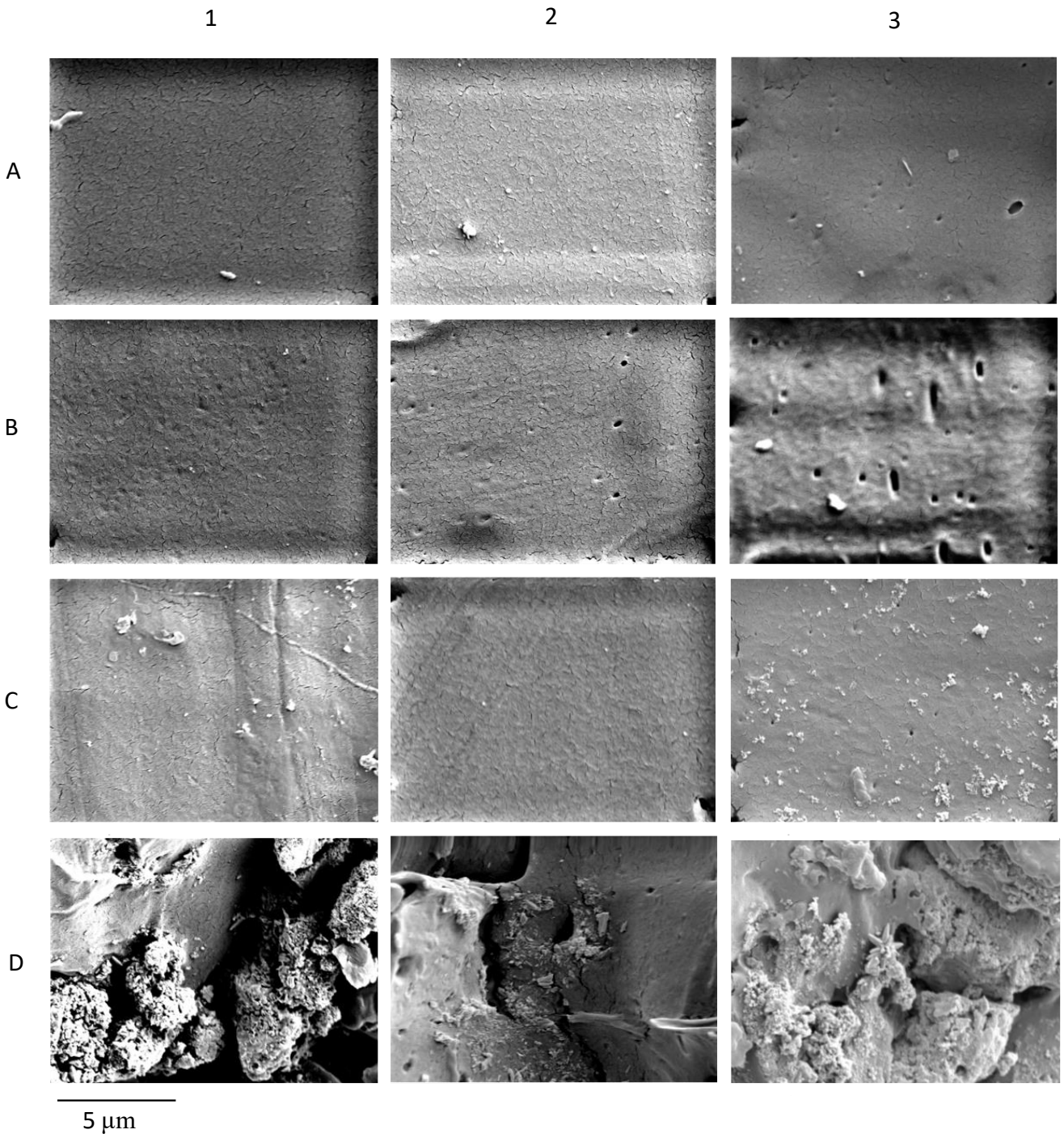


**Figure 32** – *Figure showing SEM images of the membranes at 10,000 times magnification. From columns 1-3: Aquivion®, Nafion™ and D170-U. From rows A-D: pristine membrane, used membrane (cathode side), used membrane (anode side, in contact with flow channel) and used membrane (anode side, in contact with current collectors).*

The images in row A show each membrane in pristine condition before the chronopotentiometry test. Aquivion® (1A) and Nafion™ (2A) show a uniform surface filled with thin crevices. These openings are thought to be membrane pores formed by the hydrophilic

cluster domains - however as these membranes function in the hydrated state and the images shown are under vacuum, it is unclear if this is a true representation of pore morphology. For D170-U (3A), the pristine membrane shows pinholes dispersed across the surface, indicating pre-existing damage to the membrane. This was not surprising, as the literature highlights some production processes can cause pinhole formation[150].

Row B shows the side of the membrane that was in contact with the cathode. Overall, the surfaces appear to be mostly flat, with minimal cathodic residue imprinted on to the membrane. Aquivion® (1B) appears to have undergone the least surface damage, however it could be said that early pinhole formation is evidenced by the light dimpling across the surface. Image 2B illustrates Nafion™ with several pinholes across the surface and some dimpling similar to image 1B. D170-U (3B) shows the greatest number of pinholes. All holes were present at the start of imaging, so the possibility they are the result of beam damage can be dismissed.

When looking at the membrane surface in contact with the anode, there were two distinct regions as highlighted by row C and D. Row C shows the section which was relatively clean of debris, which is thought to be the part of the membrane aligned with the flow channel. Row D shows the section which has large amounts of anodic residue imprinted into the surface of the membrane. This is thought to arise from the direct contact of the membrane, anode and raised section of the current collector (which separated the flow channels). Images 1C and 2C are comparable to that of the pristine membranes, albeit with a little more debris on the surface. Image 3C showed some evidence of pinhole formation however this was not dissimilar to the 'pristine' D170-U, indicating no greater level of pinhole formation. Image 2D appears to show some evidence of pinhole formation amongst the anode residue, however this is hard to confirm due to crowding in the image.

The literature reports that pinhole formation and membrane degradation primarily occur at the cathode side, which the images shown in Figure 32 support[151]. It should be noted that pinholes do not always permeate the full thickness of the membrane as they are the results of localised membrane thinning. This means they act to increase gas crossover in the same way using a thinner vs thicker membrane would.

Figure 32 shows that all of the membranes tested displayed some degree of damage after operation, and the images suggest this occurred the least in Aquivion® compared to Nafion™

and D170-U. However, the SEM images shown are qualitative, and to determine if damage varied significantly across each membrane, a quantitative study should be conducted. That said, the identification of damage on each membrane suggests this is what caused the system degradation observed.

Due to the initial presence of pinholes on D170-U, a fair comparison between Nafion™ and D170-U regarding pinhole formation cannot be made. Additionally, it is unclear why D170-U demonstrated comparable gas crossover to the two other membranes prior to use given that pinholes were present from the start.

The SEM images are taken on very small spot size – around 140 $\mu m^2$, which represents approximately 0.00001 % of the total surface. To take a more representative image of each sample, a lower magnification could have been used - however this would likely lead to a lack of detail. This trade off must be balanced carefully when characterising samples. Additionally, the number of samples tested was low, meaning that variation across each brand of membrane was not accounted for. If a greater number of samples were imaged, the number of pinholes across a set number of images could be totalled and averaged to provide more representative data.

#### 4.2.2.1. Causes of Membrane Degradation

Each membrane displayed some degradation after use, and the SEM images suggest this occurred to a greater extent in Nafion™ and D170-U compared to Aquivion®. To understand why this is the case, the extended structures and primary degradation mechanisms must be discussed.

Variations in the length of side chain in polymers affect something known as crystallinity – which describes the extent of order within a structure. It is known that PFSA membranes have two distinct regions – the hydrophobic PTFE-like backbone and the hydrophilic cluster phase domains which are formed by the side chains[61]. If the side chains are longer there will be less order due to an increase in repulsive forces (hydrophilic-hydrophobic interactions), and a decrease attractive forces (which help the polymer to maintain its structural integrity). If the side chains are shorter, the opposite is true. This is summarised in Figure 33.

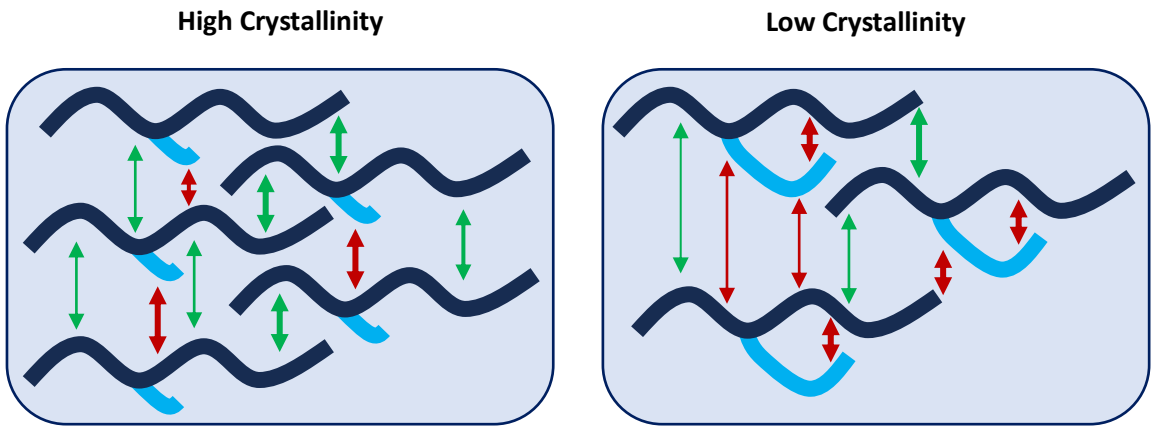


**Figure 33 –** *Schematic highlighting the differences in intermolecular forces in a polymer with high crystallinity (left) and low crystallinity (right). The red arrows indicate repulsive forces, whereas the green arrows indicate attractive forces. Arrow thickness indicates strength of interaction.*

This means that a membrane with lower crystallinity is less structurally inert, thus making it more susceptible to the three primary degradation routes – thermal, mechanical and chemical degradation[64].

Thermal damage of the membrane arises from operating the system at elevated temperatures or via the formation of local reaction hot spots. Short side chain PFSA membranes have increased thermal resistance and are known to be stable at temperatures up to 130 °C, whereas their long side chain counterparts would decompose under such conditions[57]. In this study temperatures were limited to 60 °C, so operating temperature likely did not cause the long side chain membranes to degrade.

Mechanical instability can also induce membrane degradation, and although cells are designed to mitigate this as much as possible, it cannot be fully prevented. For example, rough electrode materials can create microtears in the membrane upon assembly[27]. That said, the results show pinholes were predominantly present on the cathode side – which is a smoother surface than the anode. Pressure hot spots can also form on the surface in areas of increased stress, such as water inlet/outlets and the corners of flow channels. Over time this may cause the membrane to thin and for pinholes to form[37]. The small spot size of the SEM would make it hard to investigate the presence of this, and so an alternative imaging technique could be used.

Membranes can also degrade via a chemical reaction mechanism. In this route, hydrogen free radicals form at the cathode from hydrogen gas. These radicals then react with oxygen to form the strong oxidising agent hydrogen peroxide. Some metal cations – such as iron and copper – will be oxidised in the presence of hydrogen peroxide, thus forming more free radicals and hydroxide ions[152]. At any stage, these radicals are free to react with the surface of the membrane and wreak havoc on the extended structure[37]. Given that higher crystallinity increases chemical inertness, it is possible that this is why Aquivion® appeared to show reduced pinhole formation.

Membrane degradation is a complex multifaceted process that has many different contributions, and the primary routes are all interlinked. That said, there are a few factors which suggest chemical degradation may be the primary form of membrane degradation present in this study. The first is that cell used in this study was designed to minimise the formation of thermal/pressure hot spots, whereas the user cannot design the cell to reduce chemical damage. Further to this, chemical degradation is known to occur at the cathode side, and pinhole formation was mostly observed here.

To test for this quantitively, the fluoride concentration of the anolyte and catholyte could be measured using inductively coupled plasma-mass spectroscopy. If the results showed a higher concentration of fluorine in the catholyte than the anolyte, it would support the conclusion that chemical degradation was the main route of membrane degradation. This type of study has been reported in the literature and fluoride release rate is often reported when quantifying membrane degradation[27,146]. Not only is this analysis useful for degradation studies, but when developing 'green' technology it is important to consider the greater impact on the environment. Fluoride is toxic to many plants and animals, and its accumulation can severely disrupt entire ecosystems[153]. When considering the future broadscale use of PEM's, a lower fluoride release rate would be desirable due to the reduced impact on the surrounding environment.

### 4.3. Error

In this study, there was error which may have impacted the significance of the results gathered. Overall, it can be said the differences in results reported for each membrane are smaller than the sum of all the errors present in this study. Further repeat experiments of each membrane would reduce this, however due to time restraints this was not possible.

It is likely the primary source of this error was related to the in-house produced anode. Despite best efforts to keep the production process identical, the iridium loading masses were only accurate to one decimal place, thus leading to a maximum variation in iridium loading mass of 0.09 mg $cm^{-2}$ between trials. The catalyst surface was also deposited by hand, meaning variations may have arisen from things like time under spraying, pressure and distance from surface. This may have altered the true loading mass of iridium due to catalyst leaching into the GDL.

To mitigate this in the future, prefabricated anode catalysts could be purchased from a specialist company. Another option would be to invest in an automatic spray coater, which would allow for guaranteed standardisation of anode production. Additionally, some studies have reported ultrasonic spray coaters, which can increase efficiency of catalysts thus allowing for lower loading masses to be used[154]. However, all of these suggestions come with a notable increase in cost, which is something that limits their application in smaller laboratories.

# 5. Conclusions

The performance, stability and gas crossover of Aquivion®, Nafion™, and D170-U were evaluated and compared through a range of electrochemical, analytical and characterisation techniques. Although some variations in results were observed, overall, the membranes were found to have similar effects on device performance, degradation rate and hydrogen crossover at the anode. This suggests that varying the side chain length of the membrane used does not significantly impact PEMWE device operation. These results also demonstrate that D170-U generally performed comparably to the other two branded membranes, highlighting the suitability of the membrane for application in PEMWE research. Ex-situ characterisation revealed a lack of catalyst degradation and the presence of membrane damage, indicating this is what caused the system degradation observed.

# 6. Future Outlook

Further repeats of the experiments would reduce the error and increase the reliability of the data presented. The work reported has laid the foundation for future investigatory work on both identifying a potential replacement PEM, and also determining the effects of a short side chain vs long side chain on PEM performance.

The next steps for this research would be to perform extended studies on D170-U – either through longer chronopotentiometry tests or accelerated stress testing. This would allow an accurate determination of how the membrane performs in a real-world setting. These extended tests could be coupled with on-line gas chromatography to investigate how the rates of hydrogen crossover progress over time and relate to degradation. Identifying the primary degradation routes of each membrane would also be beneficial. Chemical degradation could be studied through fluoride release rate. The presence of thermal degradation could be identified using a high-resolution infrared camera to track thermal hot spots. These areas could then be investigated using a non-invasive imaging technique – such as SEM, atomic force or confocal microscopy - to determine if this led to an increase in membrane degradation.

Given the low stock of PFSA membranes, it would be useful to test hydrocarbon membranes and include them in this study. FuelCellStore has several different varieties of Fumasep available – each made of a different hydrocarbon backbone. By testing these membranes using the method reported, a fair comparison of PFSA vs hydrocarbon could be drawn. The hydrocarbon membranes would be hypothesised to show improved performance, but also faster rates of degradation. This may highlight the usefulness of the membranes in situations where long term testing is not necessary - such as initial performance screening of a novel catalyst.

# 7. Acknowledgements

I would like to thank Prof Mark D Symes for his support and knowledge throughout this research project. I would also like to thank Mr Abdulhai Faqeeh for the original idea of the project, in addition to all of his day-to-day support and fun times had in the lab. Additional thanks are extended to the rest of the Symes Group – specifically Zeliha Ertekin for constant support and good spirits throughout my time in the lab.

# 8. References


1. United Nations (1992). *United Nations Framework Convention on Climate Change.* New York. Available online at: https://unfccc.int/resource/docs/convkp/conveng.pdf
2. Rogelj, J. *et al.* Scenarios towards limiting global mean temperature increase below 1.5 °C. *Nat Clim Chang.* **8**, 325–332, doi: 10.1038/s41558-018-0091-3 (2018).
3. Falkner, R. The Paris Agreement and the new logic of international climate politics. *Int Aff*. **92**, 1107–1125, doi: 10.1111/1468-2346.12708 (2016).
4. World Resources Institute (2022). *Climate Watch Historical GHG Emissions*. Washington, DC. Available online at: https://www.climatewatchdata.org/ghg-emissions
5. Osman, A. I. *et al.* Cost, environmental impact, and resilience of renewable energy under a changing climate: a review. *Environ Chem Lett.* **21**, 741–764, doi: 10.1007/s10311-022-01532-8 (2023).
6. Ritchie, H., Rosado, P. & Roser, M. *Energy Production and Consumption*. Available online at: https://ourworldindata.org/energy-production-consumption (2024)
7. Friedemann, A. J. *Life after Fossil Fuels*. Springer International Publishing, 2021, vol. 81, ch. 1, pp 1-5.
8. Crew, B. Solving the energy crisis. *Nature.* **609**, S1, doi: 10.1038/d41586-022-02830-5 (2022).
9. Voldsund, M., Jordal, K. & Anantharaman, R. Hydrogen production with CO2 capture. *Int J Hydrogen Energy.* **41**, 4969–4992, doi: 10.1016/j.ijhydene.2016.01.009 (2016).
10. Zhang, B., Zhang, S.-X., Yao, R., Wu, Y.-H. & Qiu, J.-S. Progress and prospects of hydrogen production: Opportunities and challenges. *JEST.* **19**, 100080, doi: 10.1016/j.jnlest.2021.100080 (2021).
11. Bauer, C. *et al.* On the climate impacts of blue hydrogen production. *Sustain Energy Fuels.* **6**, 66–75, doi: 10.1039/D1SE01508G (2022).
12. Chatenet, M. *et al.* Water electrolysis: from textbook knowledge to the latest scientific strategies and industrial developments. *Chem Soc Rev.* **51**, 4583–4762, doi: 10.1039/D0CS01079K (2022).
13. Millet, P. *Hydrogen Production: Electrolysis*. Wiley, 2015, ch. 2, pp. 33-62.
14. O'Brien, J. E. Proceedings of the 2008 International Mechanical Engineering Congress Exposition, Boston, 2008.
15. Stratakes, B. M., Dempsey, J. L. & Miller, A. J. M. Determining the overpotential of electrochemical fuel synthesis mediated by molecular catalysts: recommended practices,

standard reduction potentials, and challenges. *ChemElectroChem.* **8**, 4161–4180, doi: 10.1002/celc.202100576 (2021).

16. Smolinka, T., Bergmann, H., Garche, J. & Kusnezoff, M. *Electrochemical Power Sources: Fundamentals, Systems, and Applications.* Elsevier, 2022, ch. 4, pp. 83-164.
17. Khan, M. A. *et al.* Recent Progresses in Electrocatalysts for Water Electrolysis. *Electrochem Energy Rev.* **1**, 483–530, doi: 10.1007/s41918-018-0014-z (2018).
18. Huang, H. *et al.* Iron-tuned super nickel phosphide microstructures with high activity for electrochemical overall water splitting. *Nano Energy.* **34**, 472–480, doi: 10.1016/j.nanoen.2017.03.016 (2017).
19. Ursua, A., Gandia, L. M. & Sanchis, P. Hydrogen production from water electrolysis: current status and future trends. *Proceedings of the IEEE.* **100**, 410–426, doi: 10.1109/JPROC.2011.2156750 (2012).
20. Xia, Y., Cheng, H., He, H. & Wei, W. Efficiency and consistency enhancement for alkaline electrolyzers driven by renewable energy sources. *Comms Eng.* **2**, 22, doi: 10.1038/s44172-023-00070-7 (2023).
21. Rashid, M., Nassem, H., Al Mesfer, M. & Danish, M. Hydrogen production by water electrolysis: a review of alkaline water electrolysis, PEM water electrolysis and high temperature water electrolysis. *IJEAT.* **4**, 80–93 (2015).
22. Haug, P., Koj, M. & Turek, T. Influence of process conditions on gas purity in alkaline water electrolysis. *Int J Hydrogen Energy.* **42**, 9406–9418, doi: 10.1016/j.ijhydene.2016.12.111 (2017).
23. Zhou, H. *et al.* Water splitting by electrolysis at high current densities under 1.6 volts. *Energy Environ Sci.* **11**, 2858–2864, doi: 10.1039/C8EE00927A (2018).
24. Aboukalam da Cruz, M. H. A. *et al.* Dynamic modelling of an alkaline water electrolysis system and optimization of its operating parameters for hydrogen production. *Int J Hydrogen Energy.* **48**, 12982–12999, doi: 10.1016/j.ijhydene.2022.12.130 (2023).
25. Shiva Kumar, S. & Himabindu, V. Hydrogen production by PEM water electrolysis – A review. *Mater Sci Energy Technol.* **2**, 442–454, doi: 10.1016/j.mset.2019.03.002 (2019).
26. Babic, U., Suermann, M., Büchi, F. N., Gubler, L. & Schmidt, T. J. Critical review—identifying critical gaps for polymer electrolyte water electrolysis development. *J Electrochem Soc*. **164**, F387–F399, doi: 10.1149/2.1441704jes (2017).
27. Feng, Q. *et al.* A review of proton exchange membrane water electrolysis on degradation mechanisms and mitigation strategies. *J Power Sources.* **366**, 33–55, doi: 10.1016/j.jpowsour.2017.09.006 (2017).

28. Liu, R.-T. *et al.* Recent advances in proton exchange membrane water electrolysis. *Chem Soc Rev.* **52**, 5652–5683, doi: 10.1039/D2CS00681B (2023).
29. Clapp, M., Zalitis, C. M. & Ryan, M. Perspectives on current and future iridium demand and iridium oxide catalysts for PEM water electrolysis. *Catal Today.* **420**, 114140, doi: 10.1016/j.cattod.2023.114140 (2023).
30. Henkensmeier, D. *et al.* Overview: State-of-the art commercial membranes for anion exchange membrane water electrolysis. *J Electrochem Energ Convers.* **18**, 024001, doi: 10.1115/1.4047963 (2021).
31. Miller, H. A. *et al.* Green hydrogen from anion exchange membrane water electrolysis: a review of recent developments in critical materials and operating conditions. *Sustain Energy Fuels.* **4**, 2114–2133, doi: 10.1039/C9SE01240K (2020).
32. Li, D. *et al.* Highly quaternized polystyrene ionomers for high performance anion exchange membrane water electrolysers. *Nat Energy.* **5**, 378–385, doi: 10.1038/s41560-020-0577-x (2020).
33. Park, J. E. *et al.* High-performance anion-exchange membrane water electrolysis. *Electrochim Acta.* **295**, 99–106, doi: 10.1016/j.electacta.2018.10.143 (2019).
34. Brauns, J. & Turek, T. Alkaline water electrolysis powered by renewable energy: a review. *Processes.* **8**, 248, doi: 10.3390/pr8020248 (2020).
35. Li, W. *et al.* Low-temperature water electrolysis: fundamentals, progress, and new strategies. *Mater Adv.* **3**, 5598–5644, doi: 10.1039/D2MA00185C (2022).
36. Carmo, M., Fritz, D. L., Mergel, J. & Stolten, D. A comprehensive review on PEM water electrolysis. *Int J of Hydrogen Energy.* **38**, 4901–4934, doi: 10.1016/j.ijhydene.2013.01.151 (2013).
37. Zhang, K. *et al.* Status and perspectives of key materials for PEM electrolyzer. *Nano Research Energy*. **1**, e9120032, doi: 10.26599/NRE.2022.9120032 (2022).
38. Lettenmeier, P. *et al.* Low-cost and durable bipolar plates for proton exchange membrane electrolyzers. *Sci Rep.* **7**, 44035, doi: 10.1038/srep44035 (2017).
39. Wang, T., Cao, X. & Jiao, L. PEM water electrolysis for hydrogen production: fundamentals, advances, and prospects. *Carbon Neutrality.* **1**, 21, doi: 10.1007/s43979-022-00022-8 (2022).
40. *Siemens Energy – Elyzer P-300.* Available online at: https://www.siemens-energy.com/global/en/home/products-services/product-offerings/hydrogen-solutions.html

41. Navarro, A. J., Gómez, M. A., Daza, L. & López-Cascales, J. J. Production of gas diffusion layers with cotton fibers for their use in fuel cells. *Sci Rep.* **12**, 4219, doi: 10.1038/s41598-022-08124-0 (2022).
42. Hussain, J. *et al.* Porous material (titanium gas diffusion layer) in proton exchange membrane fuel cell/electrolyzer: fabrication methods & amp; GeoDict: a critical review. *Materials.* **16**, 4515, doi: 10.3390/ma16134515 (2023).
43. Park, S., Lee, J.-W. & Popov, B. N. A review of gas diffusion layer in PEM fuel cells: Materials and designs. *Int J Hydrogen Energy.* **37**, 5850–5865, doi: 10.1016/j.ijhydene.2011.12.148 (2012).
44. Prando, D. *et al.* Corrosion of titanium: part 1: aggressive environments and main forms of degradation. *J Appl Biomater Funct Mater.* **15**, e291–e302, doi: 10.5301/jabfm.5000387 (2017).
45. Mathur, V. K. & Crawford, J. *Recent Trends in Fuel Cell Science and Technology.* Springer New York, 2007, ch. 4, pp. 116–128.
46. Schuler, T. *et al.* Ultrathin microporous transport layers: implications for low catalyst loadings, thin membranes, and high current density operation for proton exchange membrane electrolysis. *Adv Energy Mater.* **14**, 2302786, doi: 10.1002/aenm.202302786 (2024)
47. Polonský, J. *et al.* Anodic microporous layer for polymer electrolyte membrane water electrolysers. *J Appl Electrochem.* **47**, 1137–1146, doi: 10.1007/s10800-017-1110-1 (2017).
48. Deng, T., Huang, H., Fan, L., Xu, S. & Li, H. Porous transport layers with tic-coated microporous layers for proton exchange membrane water electrolysis. *ACS Sustain Chem Eng.* **11**, 17075–17085, doi: 10.1021/acssuschemeng.3c05256 (2023).
49. Razmjooei, F. *et al.* Increasing the performance of an anion-exchange membrane electrolyzer operating in pure water with a nickel-based microporous layer. *Joule.* **5**, 1776–1799, doi: 10.1016/j.joule.2021.05.006 (2021).
50. Bühler, M., Holzapfel, P., McLaughlin, D. & Thiele, S. From catalyst coated membranes to porous transport electrode based configurations in pem water electrolyzers. *J Electrochem Soc.* **166**, F1070–F1078, doi: 10.1149/2.0581914jes (2019).
51. Pham, C. Van, Escalera-López, D., Mayrhofer, K., Cherevko, S. & Thiele, S. essentials of high performance water electrolyzers – from catalyst layer materials to electrode engineering. *Adv Energy Mater.* **11**, 2101998, doi: 10.1002/aenm.202101998 (2021).

52. Bierling, M., McLaughlin, D., Mayerhöfer, B. & Thiele, S. Toward understanding catalyst layer deposition processes and distribution in anodic porous transport electrodes in proton exchange membrane water electrolyzers. *Adv Energy Mater.* **13**, 2203636, doi: 10.1002/aenm.202203636 (2023).
53. Hickner, M. A., Ghassemi, H., Kim, Y. S., Einsla, B. R. & McGrath, J. E. Alternative polymer systems for proton exchange membranes (PEMs). *Chem Rev.* **104**, 4587–4612, doi: 10.1021/cr020711a (2004).
54. Steele, B. C. H. & Heinzel, A. Materials for fuel-cell technologies. *Nature.* **414**, 345–352, doi: 10.1038/35104620 (2001).
55. Li, T., Shen, J., Chen, G., Guo, S. & Xie, G. Performance comparison of proton exchange membrane fuel cells with ™™ and Aquivion® perfluorosulfonic acids with different equivalent weights as the electrode binders. *ACS Omega.* **5**, 17628–17636, doi: 10.1021/acsomega.0c02110 (2020).
56. Zhao, N., Shi, Z. & Girard, F. Superior proton exchange membrane fuel cell (PEMFC) performance using short-side-chain perfluorosulfonic acid (PFSA) membrane and ionomer. *Materials.* **15**, 78, doi: 10.3390/ma15010078 (2021).
57. Li, J., Pan, M. & Tang, H. Understanding short-side-chain perfluorinated sulfonic acid and its application for high temperature polymer electrolyte membrane fuel cells. *RSC Adv.* **4**, 3944–3965, doi: 10.1039/C3RA43735C (2014).
58. Economou, N. J., O'Dea, J. R., McConnaughy, T. B. & Buratto, S. K. Morphological differences in short side chain and long side chain perfluorosulfonic acid proton exchange membranes at low and high water contents. *RSC Adv.* **3**, 19525, doi: 10.1039/c3ra41976b (2013).
59. Siracusano, S. *et al.* Performance analysis of short-side-chain Aquivion®® perfluorosulfonic acid polymer for proton exchange membrane water electrolysis. *J Memb Sci.* **466**, 1–7, doi: 10.1016/j.memsci.2014.04.030 (2014).
60. Peighambardoust, S. J., Rowshanzamir, S. & Amjadi, M. Review of the proton exchange membranes for fuel cell applications. *Int J Hydrogen Energy.* **35**, 9349–9384, doi: 10.1016/j.ijhydene.2010.05.017 (2010).
61. Zhang, H. & Shen, P. K. Recent development of polymer electrolyte membranes for fuel cells. *Chem Rev.* **112**, 2780–2832, doi: 10.1021/cr200035s (2012).
62. Zuo, Z., Fu, Y. & Manthiram, A. Novel blend membranes based on acid-base interactions for fuel cells. *Polymers (Basel).* **4**, 1627–1644, doi: 10.3390/polym4041627 (2012).

63. Choi, P., Jalani, N. H. & Datta, R. Thermodynamics and proton transport in Nafion™. *J Electrochem Soc.* **152**, E123, doi; 10.1149/1.1859814 (2005).
64. Millet, P., Ranjbari, A., de Guglielmo, F., Grigoriev, S. A. & Auprêtre, F. Cell failure mechanisms in PEM water electrolyzers. *Int J Hydrogen Energy.* **37**, 17478–17487, doi: 10.1016/j.ijhydene.2012.06.017 (2012).
65. Kuhnert, E., Hacker, V. & Bodner, M. A Review of accelerated stress tests for enhancing mea durability in pem water electrolysis cells. *Int J Energy Res.* **2023**, 1–23, 10.1155/2023/3183108 (2023).
66. Wallnöfer-Ogris, E., Poimer, F., Köll, R., Macherhammer, M.-G. & Trattner, A. Main degradation mechanisms of polymer electrolyte membrane fuel cell stacks – Mechanisms, influencing factors, consequences, and mitigation strategies. *Int J Hydrogen Energy.* **50**, 1159–1182, doi: 10.1016/j.ijhydene.2023.06.215 (2024).
67. Grigoriev, S. A., Dzhus, K. A., Bessarabov, D. G. & Millet, P. Failure of PEM water electrolysis cells: Case study involving anode dissolution and membrane thinning. *Int J Hydrogen Energy.* **39**, 20440–20446, doi: 10.1016/j.ijhydene.2014.05.043 (2014).
68. Hansen, M. K. *et al.* PEM steam electrolysis at 130 °C using a phosphoric acid doped short side chain PFSA membrane. *Int J Hydrogen Energy.* **37**, 10992–11000, doi: 10.1016/j.ijhydene.2012.04.125 (2012).
69. Kerres, J. A. Development of ionomer membranes for fuel cells. *J Memb Sci.* **185**, 3–27, doi: 10.1016/S0376-7388(00)00631-1 (2001).
70. Meegoda, J. N., Bezerra de Souza, B., Casarini, M. M. & Kewalramani, J. A. A review of PFAS destruction technologies. *Int J Environ Res Public Health.* **19**, 16397, doi: 10.3390/ijerph192416397 (2022).
71. Miyake, J. & Miyatake, K. Fluorine-free sulfonated aromatic polymers as proton exchange membranes. *Polym J.* **49**, 487–495, doi: 10.1038/pj.2017.11 (2017).
72. Smitha, B., Sridhar, S. & Khan, A. A. Solid polymer electrolyte membranes for fuel cell applications—a review. *J Memb Sci.* **259**, 10–26, doi: 10.1016/j.memsci.2005.01.035 (2005).
73. Park, J. E. *et al.* High-performance proton-exchange membrane water electrolysis using a sulfonated poly(arylene ether sulfone) membrane and ionomer. *J Memb Sci.* **620**, 118871, doi: 10.1016/j.memsci.2020.118871 (2021).
74. Klose, C. *et al.* All-Hydrocarbon MEA for PEM water electrolysis combining low hydrogen crossover and high efficiency. *Adv Energy Mater.* **10**, 1903995, doi: 10.1002/aenm.201903995 (2020).

75. Schalenbach, M., Carmo, M., Fritz, D. L., Mergel, J. & Stolten, D. Pressurized PEM water electrolysis: Efficiency and gas crossover. *Int J Hydrogen Energy.* **38**, 14921–14933, doi: 10.1016/j.ijhydene.2013.09.013 (2013).
76. Park, E. J., Arges, C. G., Xu, H. & Kim, Y. S. Membrane strategies for water electrolysis. *ACS Energy Lett.* **7**, 3447–3457, doi: 10.1021/acsenergylett.2c01609 (2022).
77. Mohamed, H. F. M. *et al.* Free volume and permeabilities of O2 and H2 in Nafion™ membranes for polymer electrolyte fuel cells. *Polymer (Guildf).* **49**, 3091–3097, doi: 10.1016/j.polymer.2008.05.003 (2008).
78. Choi, S. *et al.* Enhancing the durability of hydrocarbon-membrane-based polymer electrolyte water electrolysis using a radical scavenger-embedded interlocking interfacial layer. *J Mater Chem A Mater.* **10**, 789–798, doi: 10.1039/D1TA08222A (2022).
79. Jiao, K. *et al.* Designing the next generation of proton-exchange membrane fuel cells. *Nature.* **595**, 361–369, doi: 10.1038/s41586-021-03482-7 (2021).
80. Prats, H. & Chan, K. The determination of the HOR/HER reaction mechanism from experimental kinetic data. *Phys Chem Chem Phys.* **23**, 27150–27158, doi: 10.1039/D1CP04134G (2021).
81. Wang, S., Lu, A. & Zhong, C.-J. Hydrogen production from water electrolysis: role of catalysts. *Nano Converg.* **8**, 4, doi: 10.1186/s40580-021-00254-x (2021).
82. Guo, F. *et al.* Recent advances in ultralow-pt-loading electrocatalysts for the efficient hydrogen evolution. *Adv Sci.* **10**, 2301098, doi: 10.1002/advs.202301098 (2023).
83. Ooka, H., Huang, J. & Exner, K. S. The sabatier principle in electrocatalysis: basics, limitations, and extensions. *Front Energy Res.* **9**, 654460, doi: 10.3389/fenrg.2021.654460 (2021).
84. Liu, L. Platinum group metal free nano-catalysts for proton exchange membrane water electrolysis. *Curr Opin Chem Eng.* **34**, 100743, doi: 10.1016/j.coche.2021.100743 (2021).
85. Chen, Z. W. *et al.* Unusual Sabatier principle on high entropy alloy catalysts for hydrogen evolution reactions. *Nat Commun.* **15**, 359, doi: 10.1038/s41467-023-44261-4 (2024).
86. Cheng, N. *et al.* Platinum single-atom and cluster catalysis of the hydrogen evolution reaction. *Nat Commun.* **7**, 13638, doi: 10.1038/ncomms13638 (2016).

87. Hinnemann, B. *et al.* Biomimetic hydrogen evolution: $MoS_2$ nanoparticles as catalyst for hydrogen evolution. *J Am Chem Soc.* **127**, 5308–5309, doi: 10.1021/ja0504690 (2005).

88. McHugh, P. J., Stergiou, A. D. & Symes, M. D. Decoupled electrochemical water splitting: from fundamentals to applications. *Adv Energy Mater.* **10**, 2002453, doi: 10.1002/aenm.202002453 (2020).

89. Yuan, S. *et al.* Rational electrode design for low-cost proton exchange membrane water electrolyzers. *Cell Rep Phys Sci.* **5**, 101880, doi: 10.1016/j.xcrp.2024.101880 (2024).

90. Liang, Q., Brocks, G. & Bieberle-Hütter, A. Oxygen evolution reaction (OER) mechanism under alkaline and acidic conditions. *J Phys Energy.* **3**, 026001, doi: 10.1088/2515-7655/abdc85 (2021).

91. Ma, Q. & Mu, S. Acidic oxygen evolution reaction: mechanism, catalyst classification, and enhancement strategies. *Interdiscip Mater.* **2**, 53–90, doi: 10.1002/idm2.12059 (2023).

92. Man, I. C. *et al.* Universality in oxygen evolution electrocatalysis on oxide surfaces. *ChemCatChem.* **3**, 1159–1165, doi: 10.1002/cctc.201000397 (2011).

93. Nørskov, J. K. *et al.* Origin of the overpotential for oxygen reduction at a fuel-cell cathode. *J Phys Chem B.* **108**, 17886–17892, doi; 10.1021/jp047349j (2004).

94. Zhu, Y. *et al.* Boosting oxygen evolution reaction by creating both metal ion and lattice-oxygen active sites in a complex oxide. *Adv Mater.* **32**, 1905025, doi: 10.1002/adma.201905025 (2020).

95. Grimaud, A. *et al.* Activating lattice oxygen redox reactions in metal oxides to catalyse oxygen evolution. *Nat Chem.* **9**, 457–465, doi: 10.1038/nchem.2695 (2017).

96. Yoo, J. S., Rong, X., Liu, Y. & Kolpak, A. M. Role of lattice oxygen participation in understanding trends in the oxygen evolution reaction on perovskites. *ACS Catal.* **8**, 4628–4636, doi: 10.1021/acscatal.8b00612 (2018).

97. Qu, H.-Y., He, X., Wang, Y. & Hou, S. Electrocatalysis for the oxygen evolution reaction in acidic media: progress and challenges. *Appl Sci.* **11**, 4320, doi: 10.3390/app11104320 (2021).

98. Bernt, M. *et al.* Current challenges in catalyst development for pem water electrolyzers. *Chem Ing Tech.* **92**, 31–39, doi: 10.1002/cite.201900101 (2020).

99. Zhu, W. *et al.* Stable and oxidative charged Ru enhance the acidic oxygen evolution reaction activity in two-dimensional ruthenium-iridium oxide. *Nat Commun.* **14**, 5365, doi: 10.1038/s41467-023-41036-9 (2023).

100. Minke, C., Suermann, M., Bensmann, B. & Hanke-Rauschenbach, R. Is iridium demand a potential bottleneck in the realization of large-scale PEM water electrolysis? *Int J Hydrogen Energy.* **46**, 23581–23590, doi: 10.1016/j.ijhydene.2021.04.174 (2021).
101. Claudel, F. *et al.* Degradation mechanisms of oxygen evolution reaction electrocatalysts: a combined identical-location transmission electron microscopy and x-ray photoelectron spectroscopy study. *ACS Catal.* **9**, 4688–4698, doi: 10.1021/acscatal.9b00280 (2019).
102. Chen, Z., Duan, X., Wei, W., Wang, S. & Ni, B.-J. Electrocatalysts for acidic oxygen evolution reaction: Achievements and perspectives. *Nano Energy.* **78**, 105392, doi: 10.1016/j.nanoen.2020.105392 (2020).
103. Kwon, T. *et al.* Cobalt assisted synthesis of ircu hollow octahedral nanocages as highly active electrocatalysts toward oxygen evolution reaction. *Adv Funct Mater.* **27**, 1604688, doi: 10.1002/adfm.201604688 (2017).
104. Badam, R., Hara, M., Huang, H.-H. & Yoshimura, M. Synthesis and electrochemical analysis of novel IrO2 nanoparticle catalysts supported on carbon nanotube for oxygen evolution reaction. *Int J Hydrogen Energy.* **43**, 18095–18104, doi: 10.1016/j.ijhydene.2018.08.034 (2018).
105. Liu, X. *et al.* Restructuring highly electron-deficient metal-metal oxides for boosting stability in acidic oxygen evolution reaction. *Nat Commun.* **12**, 5676, doi: 10.1038/s41467-021-26025-0 (2021).
106. Bender, G. *et al.* Initial approaches in benchmarking and round robin testing for proton exchange membrane water electrolyzers. *Int J Hydrogen Energy.* **44**, 9174–9187, doi: 10.1016/j.ijhydene.2019.02.074 (2019).
107. US Department of Energy (2009). *Procedure for Performing PEM Single Cell Testing*. Florida. Available online at: https://www.energy.gov/eere/fuelcells/articles/procedure-performing-pem-single-cell-testing
108. European Commission, Joint Research Centre, Tsotridis, G., Pilenga, A., De Marco, G. & Malkow, T. *EU Harmonised Test Protocols for PEMFC MEA testing in single cell configurations for automotive applications.* Publications Office of the European Union, Luxembourg. doi: 10.2790/54653 (2015)
109. Zhang, H. *et al.* Standardized protocols for evaluating platinum group metal-free oxygen reduction reaction electrocatalysts in polymer electrolyte fuel cells. *Nat Catal.* **5**, 455–462, doi: 10.1038/s41929-022-00778-3 (2022).

110. European Commission, Joint Research Centre, Tsotridis, G. & Pilenga, A. *EU Harmonised Protocols for Testing of Low Temperature Water Electrolysers*. Publications Office of the European Union, Luxembourg. doi: 10.2760/502481 (2021).
111. Tomić, A. Z., Pivac, I. & Barbir, F. A review of testing procedures for proton exchange membrane electrolyzer degradation. *J Power Sources.* **557**, 232569, doi: 10.1016/j.jpowsour.2022.232569 (2023).
112. Fan, J. *et al.* Bridging the gap between highly active oxygen reduction reaction catalysts and effective catalyst layers for proton exchange membrane fuel cells. *Nat Energy.* **6**, 475–486, doi: 10.1038/s41560-021-00824-7 (2021).
113. Lazaridis, T., Stühmeier, B. M., Gasteiger, H. A. & El-Sayed, H. A. Capabilities and limitations of rotating disk electrodes versus membrane electrode assemblies in the investigation of electrocatalysts. *Nat Catal.* **5**, 363–373, doi: 10.1038/s41929-022-00776-5 (2022).
114. Cheng, N., Zhang, L., Doyle-Davis, K. & Sun, X. Single-atom catalysts: from design to application. *Electrochem Energ Rev.* **2**, 539–573, doi: 10.1007/s41918-019-00050-6 (2019).
115. Zhu, Y. *et al.* Iridium single atoms incorporated in Co3O4 efficiently catalyze the oxygen evolution in acidic conditions. *Nat Commun.* **13**, 7754, doi: 10.1038/s41467-022-35426-8 (2022).
116. Yang, X.-F. *et al.* Single-atom catalysts: a new frontier in heterogeneous catalysis. *Acc Chem Res.* **46**, 1740–1748, doi: 10.1021/ar300361m (2013).
117. Macdonald, D. D. *Transient Techniques in Electrochemistry*. Springer US, 1977, ch. 6, pp. 185–228.
118. Parker, V. D. *Comprehensive Chemical Kinetics*. Elsevier, 1986, vol. 26, ch. 3, pp. 145–202.
119. Bontempelli, G., Dossi, N. & Toniolo, R. *Reference Module in Chemistry, Molecular Sciences and Chemical Engineering.* Elsevier, 3rd edn, 2018, ch. *Voltammetry|Polarography*, pp. 218-229.
120. Browne, W. R. *Electrochemistry*. Oxford University Press, 2018, ch. 5, pp. 69-74.
121. Bontempelli, G., Dossi, N. & Toniolo, R. *Reference Module in Chemistry, Molecular Sciences and Chemical Engineering.* Elsevier, 2016, ch. *Linear Sweep and Cyclic*, pp. 1-10.

122. Lazanas, A. Ch. & Prodromidis, M. I. Electrochemical impedance spectroscopy─a tutorial. *ACS Measurement Science Au.* **3**, 162–193, doi: 10.1021/acsmeasuresciau.2c00070 (2023).
123. Randviir, E. P. & Banks, C. E. Electrochemical impedance spectroscopy: an overview of bioanalytical applications. *Anal Methods.* **5**, 1098, doi: 10.1039/c3ay26476a (2013).
124. Sanginario, A. & Hernández, S. Diagnostics of electrocatalytic systems by electrochemical impedance spectroscopy. *Curr Opin Green Sustain Chem.* **39**, 100727, doi: 10.1016/j.cogsc.2022.100727 (2023).
125. Anantharaj, S. & Noda, S. Appropriate use of electrochemical impedance spectroscopy in water splitting electrocatalysis. *ChemElectroChem.* **7**, 2297–2308, doi: 10.1002/celc.202000515 (2020).
126. Magar, H. S., Hassan, R. Y. A. & Mulchandani, A. Electrochemical impedance spectroscopy (eis): principles, construction, and biosensing applications. *Sensors.* **21**, 6578, doi: 10.3390/s21196578 (2021).
127. Stauffer, E., Dolan, J. A. & Newman, R. *Fire Debris Analysis.* Elsevier, 2008, ch. 8, pp. 235–293.
128. Forgács, E. & Cserháti, T. *Food Authenticity and Traceability.* Elsevier, 2003, ch. 9, pp. 197–217.
129. Snow, N. H. *Comprehensive Analytical Chemistry.* Elsevier, 2006, vol. 47, ch. 14, pp. 443–483.
130. Berezkin, V.G., Alishoyev, V.R. & Nemirovskaya, I.B. *Journal of Chromatography Library.* Elsevier, 1977, vol. 10, ch. 1, pp. 1-33.
131. Gordon, M. H. *Principles and Applications of Gas Chromatography in Food Analysis.* Springer US, 1990, ch. 1, pp. 11–58.
132. Wang, X. *et al.* Mechanistic reaction pathways of enhanced ethylene yields during electroreduction of CO2–CO co-feeds on Cu and Cu-tandem electrocatalysts. *Nat Nanotechnol.* **14**, 1063–1070, doi: 10.1038/s41565-019-0551-6 (2019).
133. Vernon-Parry, K. D. *III-Vs Review.* Elsevier, 2000, vol. 13, ch. 4, pp 40–44.
134. Michler, G.H. *Electron Microscopy of Polymers.* Springer Berlin Heidelberg, 2008, ch. *Scanning Electron Microscopy: an introduction*, pp. 87–120.
135. Aharinejad, S. H. & Lametschwandtner, A. *Microvascular Corrosion Casting in Scanning Electron Microscopy.* Springer Vienna, 1992, ch. 3, pp. 44–51.
136. Zhou, W., Apkarian, R., Wang, Z. L. & Joy, D. *Scanning Microscopy for Nanotechnology.* Springer New York, 2006, ch. 1, pp. 1–40.

137. Potts, P. J. *A Handbook of Silicate Rock Analysis.* Springer Netherlands, 1987, ch. 5, pp 153-197.
138. Yeung, V., Miller, D. D. & Rutzke, M. A. *Food Analysis.* Springer Link, 5th ed, 2017, ch. 9, pp. 129-150.
139. Stevens, J. E. *Handbook of Advanced Plasma Processing Techniques.* Springer Berlin, 2000, ch. 2, pp. 33–68.
140. Douvris, C., Vaughan, T., Bussan, D., Bartzas, G. & Thomas, R. How ICP-OES changed the face of trace element analysis: Review of the global application landscape. *Sci Total Environ.* **905**, 167242, doi: 10.1016/j.scitotenv.2023.167242 (2023).
141. Sahin, D. *Modern Spectroscopic Techniques and Applications.* IntechOpen, 2020, ch.1, pp 1-11.
142. Faqeeh, A. H. & Symes, M. D. A standard electrolyzer test cell design for evaluating catalysts and cell components for anion exchange membrane water electrolysis. *Electrochim Acta.* **444**, 142030, doi: 10.1016/j.electacta.2023.142030 (2023).
143. Ni, M., Leung, M. K. H. & Leung, D. Y. C. Energy and exergy analysis of hydrogen production by a proton exchange membrane (PEM) electrolyzer plant. *Energy Convers Manag.* **49**, 2748–2756, doi: 10.1016/j.electacta.2023.142030 (2008).
144. Sone, Y., Ekdunge, P. & Simonsson, D. Proton conductivity of Nafion™ 117 as measured by a four-electrode ac impedance method. *J Electrochem Soc.* **143**, 1254–1259, doi: 10.1149/1.1836625 (1996).
145. Liu, S. *et al.* Impact of SiO2 Modification on the performance of Nafion™ composite membrane. *Int J Polym Sci.* **2024**, 1–10, doi: 10.1155/2024/6309923 (2024).
146. Phan, T. T., Kim, S.-K., Islam, J., Kim, M.-J. & Lee, J.-H. Degradation analysis of polymer electrolyte membrane water electrolyzer with different membrane thicknesses. *Int J Hydrogen Energy.* **49**, 875–885, doi: 10.1016/j.ijhydene.2023.09.274 (2024).
147. Siracusano, S., Baglio, V., Van Dijk, N., Merlo, L. & Aricò, A. S. Enhanced performance and durability of low catalyst loading PEM water electrolyser based on a short-side chain perfluorosulfonic ionomer. *Appl Energy.* **192**, 477–489, doi: 10.1016/j.apenergy.2016.09.011 (2017).
148. Aßmann, P., Gago, A. S., Gazdzicki, P., Friedrich, K. A. & Wark, M. Toward developing accelerated stress tests for proton exchange membrane electrolyzers. *Curr Opin Electrochem.* **21**, 225–233, doi: 10.1016/j.coelec.2020.02.024 (2020).

149. Yu, H., Bonville, L., Jankovic, J. & Maric, R. Microscopic insights on the degradation of a PEM water electrolyzer with ultra-low catalyst loading. *Appl Catal B.* **260**, 118194, doi: 10.1016/j.apcatb.2019.118194 (2020).
150. Ding, F. *et al.* The pinhole effect on proton exchange membrane fuel cell (PEMFC) current density distribution and temperature distribution. *Appl Energy.* **342**, 121136, doi: 10.1016/j.apenergy.2023.121136 (2023).
151. Chandesris, M. *et al.* Membrane degradation in PEM water electrolyzer: numerical modeling and experimental evidence of the influence of temperature and current density. *Int J Hydrogen Energy.* **40**, 1353–1366, doi: 10.1016/j.ijhydene.2014.11.111 (2015).
152. Kuhnert, E., Heidinger, M., Sandu, D., Hacker, V. & Bodner, M. Analysis of pem water electrolyzer failure due to induced hydrogen crossover in catalyst-coated pfsa membranes. *Membranes (Basel).* **13**, 348, doi: 10.3390/membranes13030348 (2023).
153. Zuo, H. *et al.* Toxic effects of fluoride on organisms. *Life Sci.* **198**, 18–24, doi: 10.1016/j.lfs.2018.02.001 (2018).
154. Chen, Y. *et al.* Key components and design strategy for a proton exchange membrane water electrolyzer. *Small Struct.* **4**, 2200130, doi: 10.1002/sstr.202200130 (2023).